

# Dispersing Envelope around the Keplerian Circumbinary Disk in L1551 NE and its Implications for the Binary Growth

Shigehisa Takakuwa<sup>1</sup>, Kazuhiro Kiyokane<sup>2</sup>, Kazuya Saigo<sup>3</sup>, & Masao Saito<sup>4</sup>

## ABSTRACT

We performed mapping observations of the Class I protostellar binary system L1551 NE in the C<sup>18</sup>O ( $J=3-2$ ), <sup>13</sup>CO ( $J=3-2$ ), CS ( $J=7-6$ ), and SO ( $J_N=7_8-6_7$ ) lines with Atacama Submillimeter Telescope Experiment (ASTE). The ASTE C<sup>18</sup>O data are combined with our previous SMA C<sup>18</sup>O data, which show a  $r \sim 300$ -AU scale Keplerian disk around the protostellar binary system. The C<sup>18</sup>O maps show a  $\sim 20000$ -AU scale protostellar envelope surrounding the central Keplerian circumbinary disk. The envelope exhibits a northeast (blue) - southwest (red) velocity gradient along the minor axis, which can be interpreted as a dispersing gas motion with an outward velocity of  $0.3 \text{ km s}^{-1}$ , while no rotational motion in the envelope is seen. In addition to the envelope, two  $\lesssim 4000$  AU scale, high-velocity ( $\gtrsim 1.3 \text{ km s}^{-1}$ ) redshifted <sup>13</sup>CO and CS emission components are found to  $\sim 40''$  southwest and  $\sim 20''$  west of the protostellar binary. These redshifted components are most likely outflow components driven from the neighboring protostellar source L1551 IRS 5, and are colliding with the envelope in L1551 NE. The net momentum, kinetic and internal energies of the L1551 IRS 5 outflow components are comparable to those of the L1551 NE envelope, and the interactions between the outflows and the envelope are likely to cause the dissipation of the envelope and thus suppression of the further growth of the mass and mass ratio of the central protostellar binary in L1551 NE.

*Subject headings:* ISM: individual objects (L1551 NE) – ISM: molecules – stars: formation

---

<sup>1</sup>Academia Sinica Institute of Astronomy and Astrophysics, P.O. Box 23-141, Taipei 10617, Taiwan; takakuwa@asiaa.sinica.edu.tw

<sup>2</sup>Department of Astronomy, Graduate School of Science, The University of Tokyo, Hongo 7-3-1, Bunkyo-ku, Tokyo 113-0033, Japan

<sup>3</sup>Department of Physical Science, Graduate School of Science, Osaka Prefecture University, 1-1 Gakuen-cho, Naka-ku, Sakai, Osaka 599-8531, Japan

<sup>4</sup>Nobeyama Radio Observatory, National Astronomical Observatory of Japan, Minamimaki, Minamisaku, Nagano 384-1805, Japan

## 1. Introduction

The physical mechanisms to set the mass ratios of binary stars is of fundamental astrophysical importance, since more than half of main-sequence, pre-main sequence, and even protostars having masses comparable to the Sun are members of binary systems (Raghavan et al. 2010; Chen et al. 2013; Reipurth et al. 2014). Binary stars with the primary masses comparable to the solar mass exhibit a wide, essentially flat distribution of the mass ratios ( $\equiv q$ ) from  $q \sim 0.1$  to 1 (Raghavan et al. 2010; Goodwin 2013). The physical processes to reproduce such a flat distribution of the binary mass ratios are, however, still controversial.

Protostellar binary systems, precursors of main-sequence binary systems, are often surrounded by disks of molecular gas and dusts, “circumbinary disks” (hereafter CBDs) (Takakuwa et al. 2012; Tobin et al. 2013; Chou et al. 2014; Dutrey et al. 2014; Takakuwa et al. 2014; Tang et al. 2014). The radii of these CBDs range from  $\lesssim 100$  to  $\sim 500$  AU, and these CBDs often show inner emission depressions and ringlike structures. Mass accretion from these CBDs onto the central protostellar binaries has been considered as one of the key physical processes to set the binary mass ratios. Recent high-resolution observations of the CBDs have indeed detected gas flows from CBDs to the inner protostellar binaries, while the spatial resolutions are not high enough to disentangle the accretions onto the primaries and secondaries (Dutrey et al. 2014; Takakuwa et al. 2014; Tang et al. 2014). Theoretically, Bate & Bonnell (1997) and Bate (2000) have shown that from their Smoothed Particle Hydrodynamic (SPH) simulations the majority of circumbinary materials accrete onto the secondary. High-resolution grid-based simulations by Ochi et al. (2005) and Hanawa et al. (2010) have shown the opposite results, that is, the primary accretes more than the secondary. Ochi et al. (2005) and Hanawa et al. (2010) argued that high-resolution simulations to sufficiently resolve the gas motions near the L2 and L3 Lagrangian points are essential to properly trace the mass accretion, since accreting gas flows into the binary through these Lagrangian points. On the other hand, latest SPH simulations have demonstrated that mass accretion in CBDs is a function of gas temperatures, and in the case of the high temperature the primary accretes more than the secondary, and vice versa (Young et al. 2015). Young et al. (2015) argued that the difference between the above results can simply be explained by the difference of the adopted gas temperatures in the models. It has been still controversial to construct a consistent, unified model of mass accretion from CBDs onto protostellar binaries.

CBDs in protostellar binary systems are considered to be embedded in larger-scale protostellar envelopes, which can replenish the central CBDs with fresh materials (Momose et al. 1998; Chou et al. 2014). Since the observed masses of CBDs around protostellar binaries ( $\lesssim 0.1 M_{\odot}$ ) are much smaller than the masses of the central protostellar binaries (Takakuwa et al. 2012; Tobin et al. 2013; Chou et al. 2014), further supply of materials from the protostellar en-

velopes to the CBDs is essential to significantly change the mass and mass ratios of the protostellar binaries. If a protostellar envelope keeps supplying materials to the central CBD, further growth of the mass and the mass ratio of the protostellar binary will be expected. On the other hand, if the most of the envelope materials are being dissipated, the present mass and mass ratio of the protostellar binary will be close to the final values. Such dissipations of protostellar envelopes through the interactions with the associated outflows or stellar winds have been investigated observationally (Kitamura et al. 1996; Momose et al. 1996; Fuente et al. 2002; Takakuwa et al. 2003; Arce & Sargent 2006; Takahashi et al. 2006). Thus, in addition to physics of accretion from CBDs onto the protostellar binaries, mass replenishment from the surrounding protostellar envelopes, and the connection between protostellar envelopes and CBDs, must be taken into account.

In the present paper, we focus on a protostellar envelope harboring the protostellar binary system L1551 NE. L1551 NE is a young Class I protostellar binary ( $T_{bol}=91$  K,  $L_{bol}=4.2 L_{\odot}$ ; Froebrich 2005) located to  $\sim 2'.5$  northeast of another, brightest protostellar binary L1551 IRS 5 in the L1551 region (Saito et al. 2001; Reipurth et al. 2002; Takakuwa et al. 2004; Hayashi & Pyo 2009; Chou et al. 2014). The protostellar binary consists of the northwestern source named “Source A”, and the southeastern source “Source B”, with the projected separation of  $\sim 70$  AU at a position angle of  $300^{\circ}$  (Reipurth et al. 2002; Takakuwa et al. 2014). Our previous SMA observations of L1551 NE have identified a  $r \sim 300$  AU scale CBD in Keplerian rotation with a central stellar mass of  $0.8 M_{\odot}$  (Takakuwa et al. 2012), plus a possible outer infalling component (Takakuwa et al. 2013). Our subsequent ALMA Cycle 0 observation of L1551 NE (Takakuwa et al. 2014), at a spatial resolution that is  $\sim 1.6$  times higher (in beam area) and a sensitivity that is  $\sim 6$  times better (in brightness temperature) than those attained in our previous SMA observations, unveiled substructures of the CBD in the 0.9-mm dust-continuum emission. The revealed substructures are consistent with our 3-D adaptive mesh refinement (AMR) hydrodynamic simulation (Matsumoto 2007) for the presence of two spiral arms driven by gravitational torques from the central binary system. The ALMA data of L1551 NE in the  $C^{18}O$  (3–2) line also exhibits the deviations from the Keplerian motion in the CBD, consistent with our AMR simulation that gravitational torques impart angular momentum along the spiral arms (driving material outwards) and extract angular momentum between the spiral arms (driving infall). Our theoretical model which reproduces the observed features of the CBD around L1551 NE predicts that secondary accretes more than the primary. Since our series of the SMA and ALMA observations of L1551 NE have revealed the CBD + protostellar binary system, the next question is the connection from the protostellar envelope to the CBD, and the mass replenishment from the envelope to the CBD.

We conducted single-dish mapping observations of the protostellar envelope surrounding

the protostellar binary system of L1551 NE in the  $\text{C}^{18}\text{O}$  ( $J=3-2$ ),  $^{13}\text{CO}$  ( $J=3-2$ ), CS ( $J=7-6$ ), and the SO ( $J_N=7_8-6_7$ ) lines with the Atacama Submillimeter Telescope Experiment (ASTE) 10-m telescope. The ASTE mapping data in the  $\text{C}^{18}\text{O}$  line are combined with our previous SMA data in the same line, which have a larger field of view and a shorter spacing than those of the ALMA data and thus more suitable to study the connection between the extended protostellar envelope and the CBD. In this paper we report these ASTE+SMA results of the protostellar envelope in L1551 NE. The structure of this paper is as follows. In section 2, our new ASTE observations, as well as the process to combine the ASTE mapping data with the SMA data in the  $\text{C}^{18}\text{O}$  line, are described. In section 3, the results of the ASTE mapping observations and the combination of the ASTE + SMA data are presented. In section 4, gas motions and physical properties of the identified gas components are estimated. In section 5, we discuss implications of the observed features in the context of growth of protostellar binaries, and concise summary is written in section 6.

## 2. ASTE Observations

We performed observations of L1551 NE in the  $\text{C}^{18}\text{O}$  ( $J=3-2$ ; 329.3305453 GHz),  $^{13}\text{CO}$  ( $J=3-2$ ; 330.587965 GHz), SO ( $J_N=7_8-6_7$ ; 340.71416 GHz), and the CS ( $J=7-6$ ; 342.882857 GHz) lines with the ASTE 10-m telescope on 2013 September 23-26 and October 4. Remote observations were performed from the ASTE operation room of NAOJ at Mitaka, Japan, using the network observation system N-COSMOS3 developed by NAOJ (Kamazaki et al. 2005). A cartridge-type, double-sideband 350 GHz receiver with an IF frequency range of 4.5 to 7 GHz (CATS345) mounted on ASTE (Kohnno 2005) was used, and all the four lines were observed simultaneously, except that on September 23 only the SO and CS lines were observed due to the mistake of the instrumental setting. We used only the data with the DSB system noise temperature ranging  $\sim 200$  - 800 K, and the data with the higher noise temperatures are excluded. The telescope pointing was checked every  $\sim 1.5$  - 2 hours by five-point CO ( $J = 3-2$ ) observations of a late-type star, NML-Tau, and was found to be better than  $\sim 2''$ . As a standard source we also observed Orion KL (Schilke et al. 1997) and L1551 IRS 5 (Takakuwa & Kamazaki 2011), and confirmed that the relative intensity was consistent within  $\sim 30\%$  with a main beam efficiency of 0.6. No further correction for the sideband ratio was performed. Hereafter we show the observed line intensities in the unit of  $T_{MB}$ .

The observations consisted of two parts; one-point, deep observations toward the center of L1551 NE ( $\alpha_{J2000}, \delta_{J2000}$ ) = ( $04^h31^m44^s.47$ ,  $18^\circ08'32''.2$ ), which is the field center of our previous SMA observations and matches approximately the positions of the protostellar binary

(Takakuwa et al. 2012; Takakuwa et al. 2013), and mapping observations around L1551 NE. Both observations were conducted in the position-switching mode. The SO and CS line data toward the center of L1551 NE taken on September 23, when the other line data were not taken due to the mistake of the instrumental setting, are included in the deep integrations. The resultant total on-source integration times of the SO and CS data toward the center of L1551 NE is 1620 sec, while those of the  $^{13}\text{CO}$  and  $\text{C}^{18}\text{O}$  data 1220 sec. The rms noise levels of the  $^{13}\text{CO}$ ,  $\text{C}^{18}\text{O}$ , SO, and the CS spectra toward the center of L1551 NE are 0.055 K, 0.062 K, 0.025 K, and 0.029 K, respectively. The mapping observations were conducted with a grid spacing of  $10''$  (Nyquist sampling), and a typical on-source integration time per point of  $\sim 80$  seconds. The map center is set to be the position of the deep integrations. The spatial and spectral resolutions and the noise level of the mapping observations in the  $\text{C}^{18}\text{O}$  line are summarized in Table 1.

We combined the ASTE image cube in the  $\text{C}^{18}\text{O}$  line with the interferometric  $\text{C}^{18}\text{O}$  data of L1551 NE taken with the SMA in its subcompact and compact configurations (Takakuwa et al. 2013), adopting the method described by Takakuwa et al. (2007b). Details of the SMA observations are described by Takakuwa et al. (2013). The conversion factor from  $T_{MB}$  (K) to  $S$  ( $\text{Jy beam}^{-1}$ ) was derived to be 48.5 as

$$S = \frac{2k_B\Omega_{beam}}{\lambda^2}T_{MB}, \quad (1)$$

where  $k_B$  is the Boltzmann constant,  $\lambda$  is the wavelength, and  $\Omega_{beam}$  is the solid angle of the ASTE beam ( $= 23''$ ). The spatial and spectral resolutions and the noise level of the combined SMA+ASTE image cube in the  $\text{C}^{18}\text{O}$  line are summarized in Table 1.

### 3. Results

#### 3.1. ASTE Spectra toward L1551 NE

Figure 1 shows the observed ASTE spectra of the  $\text{C}^{18}\text{O}$  ( $J=3-2$ ),  $^{13}\text{CO}$  ( $J=3-2$ ), CS ( $J=7-6$ ), and the SO ( $J_N=7_8-6_7$ ) lines toward the protobinary of L1551 NE. The  $\text{C}^{18}\text{O}$  spectrum appears to consist of narrow and wide components. Two-component Gaussian fitting to the  $\text{C}^{18}\text{O}$  spectrum shows that the peak brightness temperature, line width, and the centroid velocity of the narrow component are 2.4 K,  $0.72 \text{ km s}^{-1}$ , and  $6.68 \text{ km s}^{-1}$ , and those of the wide component 1.1 K,  $2.24 \text{ km s}^{-1}$ , and  $6.99 \text{ km s}^{-1}$ , respectively (light lines in Figure 1). Previous CSO observations also found that the  $\text{C}^{18}\text{O}$  ( $3-2$ ) spectrum toward L1551 NE can be decomposed of two Gaussian components with similar line widths and centroid velocities (Fuller & Ladd 2002). In particular, the centroid velocity of the broad

component is similar to the centroid velocity of the CBD derived from our previous SMA observations ( $= 6.9 \text{ km s}^{-1}$ ) (Takakuwa et al. 2012; Takakuwa et al. 2013). As shown in the next subsection, the broad  $\text{C}^{18}\text{O}$  component is present only toward the protobinary position. These results indicate that the broader component in the ASTE  $\text{C}^{18}\text{O}$  spectrum likely originates from the central CBD. On the other hand, the narrower  $\text{C}^{18}\text{O}$  component traces a distinct component at a slightly blueshifted ( $\sim 0.2 \text{ km s}^{-1}$ ) centroid velocity. As shown below, this narrow component traces the extended envelope component around L1551 NE. Hereafter in this paper,  $V_{LSR} = 6.7 \text{ km s}^{-1}$  is adopted as the systemic velocity of the extended envelope component, while  $V_{LSR} = 6.9 \text{ km s}^{-1}$  as the systemic velocity of the CBD in L1551 NE.

The  $^{13}\text{CO}$  ( $J=3-2$ ) spectrum shows an absorption dip at around the centroid velocity of the narrow component of the  $\text{C}^{18}\text{O}$  spectrum, and a broad redshifted wing up to  $V_{LSR} \sim 13 \text{ km s}^{-1}$ . While a part of the redshifted wing in the  $^{13}\text{CO}$  spectrum likely originates from the CBD as in the case of the  $\text{C}^{18}\text{O}$  spectrum, mapping observations of the  $^{13}\text{CO}$  line demonstrate that the redshifted  $^{13}\text{CO}$  emission is most likely arising from the outflow component driven from L1551 IRS 5, as will be discussed below. With a deeper integration a much better CS ( $J=7-6$ ) spectrum of L1551 NE than our previous one (Takakuwa & Kamazaki 2011) is obtained. The CS spectrum shows a non-Gaussian, flat-top spectral shape. Whereas the SO ( $J_N=7_8-6_7$ ) line is weak compared to the other lines, the peak intensity ( $\sim 0.14 \text{ K}$ ) is detected above  $5.5\sigma$ .

### 3.2. Spatial and Velocity Distributions Observed with ASTE

Figure 2 shows total integrated intensity maps of the four molecular lines observed with ASTE. The  $\text{C}^{18}\text{O}$  ( $3-2$ ) emission exhibits condensed and diffuse components, the former of which is centered on the protobinary position. Two-component, two-dimensional Gaussian fitting to the  $\text{C}^{18}\text{O}$  total integrated map shows that the  $\text{C}^{18}\text{O}$  emission can be decomposed of a central component with a size of  $\sim 5500 \text{ AU} \times 2600 \text{ AU}$  (P.A. $=-46^\circ$ ) and a diffuse component with a size of  $\sim 21000 \text{ AU}$ . Emission peaks toward the protostellar position are also seen in the CS ( $7-6$ ) and SO ( $7_8-6_7$ ) lines. On the other hand, the  $^{13}\text{CO}$  ( $3-2$ ) peak emission does not coincide with the protostellar position but is offset at  $\sim 20''$  west from the protostar. The  $^{13}\text{CO}$  emission shows an elongated feature toward the southwest direction, which is also evident in the  $\text{C}^{18}\text{O}$  and CS emission.

Figure 3 shows the ASTE velocity channel maps of the  $^{13}\text{CO}$  line at a velocity interval of  $0.455 \text{ km s}^{-1}$ . In the blueshifted velocity range ( $V_{LSR}=4.62 - 5.99 \text{ km s}^{-1}$ ), an emission component to the northwest of the protostar and that centered on the protostellar position

are seen. Around the systemic velocity ( $6.45 - 6.90 \text{ km s}^{-1}$ ) the  $^{13}\text{CO}$  line shows less intensity contrast, suggesting that the  $^{13}\text{CO}$  emission traces the overall cloud component. In the redshifted velocity of  $7.36 - 9.18 \text{ km s}^{-1}$ , two emission components, one located to  $\sim 20''$  west of the protostar, and the other to  $\sim 40''$  southwest, are seen. While the southwestern component diminishes at velocities higher than  $9.63 \text{ km s}^{-1}$ , the western component is seen until  $\sim 12.36 \text{ km s}^{-1}$ . The location and velocity of this high-velocity redshifted component is consistent with those of a redshifted outflow component seen in the  $^{12}\text{CO}$  (1–0; 2–1; 3–2) lines (Stojimirović et al. 2006; Moriarty-Schieven et al. 2006) and the CS (2–1; 3–2) lines (Plambeck et al. 1995; Yokogawa et al. 2003) driven from the neighboring protostellar source, L1551 IRS 5. Thus, the high-velocity redshifted component seen in the  $^{13}\text{CO}$  line most likely traces the redshifted outflow component from L1551 IRS 5.

Figure 4 shows the ASTE velocity channel maps of the  $\text{C}^{18}\text{O}$  line at the same velocity bin as that of the  $^{13}\text{CO}$  velocity channel maps. The  $\text{C}^{18}\text{O}$  emission component associated with the protostar is seen from  $V_{\text{LSR}} = 5.53 \text{ km s}^{-1}$ . The  $\text{C}^{18}\text{O}$  emission component exhibits an elongated feature at  $6.44 - 6.90 \text{ km s}^{-1}$  along the northwest to the southeast direction, which is approximately consistent with the major axis of the central disk. While the  $\text{C}^{18}\text{O}$  emission peak at  $6.44 \text{ km s}^{-1}$  is located to the northeast of the protostar, the emission location is systematically shifted from northeast to southwest from the blueshifted to redshifted velocities ( $6.44 \text{ km s}^{-1}$  to  $7.81 \text{ km s}^{-1}$ ). These results indicate that there is a velocity gradient in the  $\text{C}^{18}\text{O}$  emission along the direction of the minor axis of the central disk. These  $\text{C}^{18}\text{O}$  emission components most likely trace the protostellar envelope surrounding L1551 NE (hereafter “ENV”). In the redshifted velocities from  $7.35 \text{ km s}^{-1}$ , another emission component to the southwest of the protostar becomes evident. This component appears to trace the same southwestern gas component seen in the  $^{13}\text{CO}$  emission. In even higher redshifted velocities ( $8.72 - 10.54 \text{ km s}^{-1}$ ), the  $\text{C}^{18}\text{O}$  counterpart of the western redshifted component found in the  $^{13}\text{CO}$  emission is also seen, although the highest velocity end of the  $\text{C}^{18}\text{O}$  counterpart is lower than that of the  $^{13}\text{CO}$  emission.

Figure 5 shows the same velocity channel maps as those of Figures 3 and 4 but for the CS (7–6) line. While the CS emission traces a gas component associated with the protostar in the velocity range of  $5.54 - 7.81 \text{ km s}^{-1}$ , the most prominent CS emission component is the redshifted ( $8.27 - 9.18 \text{ km s}^{-1}$ ) component to the southwest of the protostar. This southwestern redshifted component is also seen in the  $^{13}\text{CO}$  and  $\text{C}^{18}\text{O}$  emission. Previous BIMA and NMA observations of the CS (2–1; 3–2) lines have also found the same CS component, where the CS abundance is enhanced by a factor of a few (Plambeck et al. 1995; Yokogawa et al. 2003). This CS component is considered to be shock-excited molecular gas of the outflow driven from L1551 IRS 5 (Plambeck et al. 1995). The detection of the submillimeter CS (7–6) emission with the present ASTE observations, which traces warm ( $\gtrsim$

60 K) molecular gas (Takakuwa et al. 2007a; Takakuwa & Kamazaki 2011), further supports this interpretation. Hereafter we call this redshifted component to the southwest of the protostar “RED1”, and the highest-velocity redshifted component seen in the  $^{13}\text{CO}$  and  $\text{C}^{18}\text{O}$  lines to the west of the protostar “RED2”.

In Figure 6, we compare spatial distributions of ENV as seen in the  $\text{C}^{18}\text{O}$  emission, RED1 in the CS emission, and RED2 in the  $^{13}\text{CO}$  emission. Line profiles in the peak positions of RED1 and RED2, as well as those 20'' east of the protostar, are also shown (Note that the line profiles of ENV are shown in Figure 1.). The two outflow components of RED1 and RED2 are located to the western side of ENV. Toward RED1, the  $^{13}\text{CO}$  line profile shows an intense redshifted peak plus a red wing up to  $V_{\text{LSR}} \sim 12 \text{ km s}^{-1}$ . The  $\text{C}^{18}\text{O}$  line profile exhibits redshifted emission “plateau” up to  $V_{\text{LSR}} \sim 10 \text{ km s}^{-1}$ , and the CS line profile shows the emission only in the redshifted velocity range. Similar  $^{13}\text{CO}$  redshifted wing and  $\text{C}^{18}\text{O}$  emission plateau are also seen toward RED2, where a weak redshifted CS emission is also present. On the other hand, toward the 20'' east of the protostar, such a  $\text{C}^{18}\text{O}$  emission plateau is not seen and the  $^{13}\text{CO}$  redshifted wing is much less prominent, and the submillimeter CS emission is not detected. These results imply that the outflow streams of RED1 and RED2 are terminated at the western side of ENV. One possible interpretation for this termination is the collision between the outflow components and ENV.

In Figure 7, we show the Position-Velocity (P-V) diagrams of the  $^{13}\text{CO}$ ,  $\text{C}^{18}\text{O}$ , and the CS lines along the cuts passing through the protostellar position and the peak positions of RED1 (P.A. =  $45^\circ$ ) and RED2 (P.A. =  $90^\circ$ ). In the  $\text{C}^{18}\text{O}$  P-Vs the envelope component is seen as labeled. To the west of ENV the  $^{13}\text{CO}$ ,  $\text{C}^{18}\text{O}$ , and the CS emission components arising from RED1, and the  $^{13}\text{CO}$  and  $\text{C}^{18}\text{O}$  emission components from RED2, can be identified. There appears velocity gradients both in RED1 and RED2 as delineated by dashed lines, and the velocities of RED1 and RED2 become closer to the systemic velocity as the positions become closer to ENV. These results suggest that the flow velocities of RED1 and RED2 are decelerated as they become close to ENV, presumably due to the collision with ENV.

Figure 8 shows ASTE P-V diagrams of the  $\text{C}^{18}\text{O}$  and  $^{13}\text{CO}$  lines along the major and minor axes of the central CBD passing through the protostellar position. In the  $\text{C}^{18}\text{O}$  P-Vs, the line broadening at the protostellar position arising from the CBD is clearly seen, and the velocity gradient originated from the Keplerian rotation (blue curves in Figure 8) can be identified along the major axis. As discussed in the  $\text{C}^{18}\text{O}$  line profile toward the protostellar position (Figure 1), the centroid velocity of the CBD component and that of the envelope component are offset by  $\sim 0.2 \text{ km s}^{-1}$  (two vertical dashed lines in Figure 8), and the  $\text{C}^{18}\text{O}$  P-Vs exhibit this offset clearly. Furthermore, along the major axis the envelope component as seen in the  $\text{C}^{18}\text{O}$  emission does not show any noticeable velocity gradient, and the Keplerian



rotation of the central disk is not continuous to the outer envelope. On the other hand, along the minor axis the  $\text{C}^{18}\text{O}$  envelope shows a clear velocity gradient along the northeast (blue) to southwest (red) direction (tilted black dashed line in Figure 8). Since the associated NIR jets are blueshifted to the southwest and redshifted to the northeast (Hayashi & Pyo 2009), the southwestern side of the disk and envelope must be far-side and the northeastern side near-side, assuming that the midplane of the disk and envelope is perpendicular to the axis of the jets. Correspondingly, the southwestern redshifted component would then be located on the far side and the northeastern blueshifted component on the near side, suggesting the outward radial motion on the plane. In the  $^{13}\text{CO}$  P-V diagram along the minor axis, both RED1 and RED2 and their decelerated velocity structures (red and pink dashed lines) are identified. These results indicate that the envelope is being dissipated due to the interaction with the redshifted outflowing gas driven from L1551 IRS 5. We will further discuss this dispersing motion of the envelope with the combined SMA+ASTE images of the  $\text{C}^{18}\text{O}$  emission below.

### 3.3. Spatial and Velocity Structures of the Inner Envelope and Circumbinary Disk traced by the SMA+ASTE $\text{C}^{18}\text{O}$ (3–2) Image Cube

Figure 9 compares moment 0 maps of the ASTE, SMA, and the combined SMA+ASTE image cubes of the  $\text{C}^{18}\text{O}$  (3–2) line in L1551 NE. While the ASTE image exhibits an extended envelope structure as described in the last subsection, the SMA image shows the central smaller-scale ( $\sim 1000 \text{ AU} \times 800 \text{ AU}$ ) structure with its position angle ( $\sim 167^\circ$ ) consistent with that of the Keplerian CBD (Takakuwa et al. 2013). Combining these two images shows that the central structure found by the SMA observations is embedded in the more extended envelope.

Figure 10 shows velocity channel maps of the SMA+ASTE image cube of the  $\text{C}^{18}\text{O}$  (3–2) line. In the highly blueshifted ( $V_{\text{LSR}} = 4.2 - 6.1 \text{ km s}^{-1}$ ) and redshifted ( $7.5 - 9.2 \text{ km s}^{-1}$ ) velocities, compact  $\text{C}^{18}\text{O}$  emission located to the north and south of the protostellar binary are seen, respectively. These compact components trace the Keplerian CBD as we already discussed in our previous papers (Takakuwa et al. 2012; Takakuwa et al. 2013; Takakuwa et al. 2014). The extended envelope component appears in the lower velocity range ( $6.1 - 8.2 \text{ km s}^{-1}$ ). In the blueshifted velocity range of  $6.3 - 6.6 \text{ km s}^{-1}$ , the extended  $\text{C}^{18}\text{O}$  emission is located predominantly to the eastern side of the protostellar binary, whereas in the redshifted velocity range of  $7.5 - 8.2 \text{ km s}^{-1}$  to the western side. Thus, there is a velocity gradient along the east (blue) to west (red) direction in the envelope, which is also identified in the ASTE only  $\text{C}^{18}\text{O}$  image cube as discussed in the last subsection. In the lower velocity region ( $6.6 - 7.4 \text{ km s}^{-1}$ ) the envelope emission extends over the entire region.

To highlight these velocity structures in the SMA+ASTE image cube, we integrated the velocity channel maps over the high-velocity, middle-velocity, and the low-velocity blueshifted and redshifted regions, and the resultant images are shown in Figure 11. In the high-velocity region, compact blueshifted and redshifted  $\text{C}^{18}\text{O}$  emission located to the north and south of the protostellar binary, which originates from the Keplerian CBD, are seen. In the middle-velocity region, as well as the central disk component, an extended envelope component, with the blueshifted emission located predominantly to the east and the redshifted emission to the west, are seen. As we discussed in the last subsection, one interpretation of this velocity structure is the dispersing gas motion in the flattened envelope. In the low-velocity region both the blueshifted and redshifted emission spread over almost the entire field of view. We note, however, that the blueshifted and redshifted emission peaks in the central compact emission are located slightly to the west and east of the protostellar binary, respectively. The sense of this velocity structure is opposite to that of the extended envelope seen in the middle velocity range. This velocity structure is also seen in the SMA only image cube and the centroid velocity of this velocity feature matches with that of the CBD. As discussed in our previous paper (Takakuwa et al. 2013), one interpretation for this velocity structure is an infalling gas motion in the inner envelope toward the central CBD. Such coexistence of inner infall and outer dispersing motions has also been identified in an envelope surrounding a T-Tauri star DG Tauri (Kitamura et al. 1996).

Figure 12 (left) shows the P-V diagrams of the combined SMA+ASTE image cube of the  $\text{C}^{18}\text{O}$  line along the major (upper panel) and minor axes (lower) of the CBD. For comparison, Keplerian rotation curves derived from the SMA data (Takakuwa et al. 2012) are drawn in black lines, and the centroid velocity of the CBD and the envelope in vertical dashed lines. In the P-V along the major axis, the central compact component, CBD, exhibits a velocity gradient consistent with the Keplerian rotation. On the other hand, the extended envelope component does not show any clear velocity gradient along the major axis, and the offset of the centroid velocity of the envelope from that of the CBD is clearly seen. These results indicate that the Keplerian rotation of the central CBD is discontinuous to the outer envelope. In the P-V diagram along the minor axis, the central component exhibits a wide velocity width but no velocity gradient, as expected from the Keplerian rotation. On the other hand, along the minor axis the emission ridges in the envelope component are located predominantly to the northeast in the blueshifted velocities, and to the southwest to the redshifted velocities, as seen in the middle velocity ranges of Figure 11. This velocity structure can be interpreted as the dispersing gas motion in the flattened envelope. We will interpret these detected velocity structures of the combined SMA+ASTE  $\text{C}^{18}\text{O}$  image cube with our toy model below.

## 4. Analyses

### 4.1. Toy Model for the Combined SMA+ASTE Image Cube

The combined SMA+ASTE C<sup>18</sup>O image cube reveals a sign of an outer dispersing envelope motion, possible inner infalling motion, and Keplerian rotation in the central CBD. To interpret these results quantitatively, we constructed a toy model of the envelope and disk assuming that the disk and envelope are geometrically thin and co-planar. Our model is essentially the same as that by Takakuwa et al. (2013), which reproduces the velocity structures of the SMA only image cube, but now the outer dispersing envelope component is added to reproduce the velocity structure of the extended envelope component traced by ASTE. As a model moment 0 map, we adopted a combination of two 2-dimensional Gaussians, which are derived from the Gaussian fitting to the observed SMA+ASTE moment 0 map (Figure 9 bottom-right). The velocity structures in the inner component traced by the SMA are described as,

$$v_{rot}(r) = \sqrt{\frac{GM_{\star}}{r}} \quad \text{and} \quad v_{rad}(r) = 0 \quad \text{for} \quad r \leq r_{kep}, \quad (2a)$$

$$v_{rot}(r) = 0 \quad \text{and} \quad v_{rad}(r) = v_{inf} \quad \text{for} \quad r > r_{kep}, \quad (2b)$$

where  $r$  is the radius,  $G$  the gravitational constant,  $M_{\star}$  the mass of the protostellar binary,  $v_{rot}(r)$  and  $v_{rad}(r)$  are the rotational and radial velocities, respectively,  $r_{kep}$  the outermost radius of the Keplerian rotation, and  $v_{inf}$  an adopted constant infall velocity beyond  $r_{kep}$ . As discussed by Takakuwa et al. (2013), we adopt  $M_{\star} = 0.8 M_{\odot}$ ,  $r_{kep} = 300$  AU, and  $v_{inf} = -0.6$  km s<sup>-1</sup>, and the disk inclination angle  $i = 62^{\circ}$ . The velocity structure of the outer envelope traced by ASTE is expressed as,

$$v_{rot}(r) = 0 \quad \text{and} \quad v_{rad}(r) = v_{disp} \quad \text{for} \quad r > r_{disp}, \quad (3)$$

where  $r_{disp}$  and  $v_{disp}$  are the innermost radius of the dispersing envelope and the dispersing velocity, respectively.  $r_{disp} = 700$  AU is adopted, inferred from the comparison between the SMA only and SMA+ASTE moment 0 maps.  $v_{disp}$  can be roughly estimated from the velocity gradient seen in the combined P-V diagram along the minor axis as shown in Figure 12. The velocity shift of the emission ridge of the envelope across the minor axis is  $\sim 0.5$  km s<sup>-1</sup>, centered on the centroid velocity of 6.7 km s<sup>-1</sup>, and at an inclination of  $i \sim 62^{\circ}$  the dispersing velocity along the flattened envelope is  $v_{disp} \sim (0.5 \text{ km s}^{-1} / 2) / \sin 62^{\circ} \sim 0.3$  km s<sup>-1</sup>. Note that the centroid velocity of the envelope component is offset by  $\sim -0.2$  km s<sup>-1</sup> from that of the CBD, and in our model this offset of the centroid velocity is incorporated. The internal velocity dispersion  $\sigma_{gas} = 0.4$  km s<sup>-1</sup>, which reproduces the velocity channel maps of the central CBD (Takakuwa et al. 2012), is adopted throughout the entire components.

Figure 13 shows the velocity channel maps of our toy model. In the high-velocity blueshifted ( $4.6 - 5.7 \text{ km s}^{-1}$ ) and redshifted ranges ( $7.7 - 9.2 \text{ km s}^{-1}$ ) the features of the Keplerian CBD are seen. In the blueshifted range of  $5.9 - 6.3 \text{ km s}^{-1}$  the envelope component is located to the east of the protostellar binary while in the redshifted range of  $7.2 - 7.5 \text{ km s}^{-1}$  to the west, reflecting the dispersing motion in the envelope. In the lower-velocity range ( $6.4 - 7.0 \text{ km s}^{-1}$ ) the envelope component is extended both in the eastern and western sides, but the east (red) - west (blue) velocity gradient arising from the infalling motion in the central component is evident. These characteristics reproduces primary features of the observed SMA+ASTE  $\text{C}^{18}\text{O}$  velocity channel maps in L1551 NE (Figure 10, 11). Figure 12 (right) shows the P-V diagrams of our toy model along the major and minor axes. The model P-Vs can reproduce primary features of the observed P-Vs, such as the high-velocity component arising from the Keplerian disk, and the extended envelope component which shows a velocity gradient along the minor axis reflecting the dispersing motion, but no rotation along the major axis. These results show that the observed SMA+ASTE  $\text{C}^{18}\text{O}$  image cube in L1551 NE can be understood with three distinct velocity components; a central Keplerian CBD at a radius of  $\lesssim 300 \text{ AU}$ , a possible infalling region at  $300 \text{ AU} < r < 500 \text{ AU}$ , and an outer dispersing envelope with a dispersing velocity of  $\sim 0.3 \text{ km s}^{-1}$  at  $r \gtrsim 500 \text{ AU}$ .

#### 4.2. Physical Properties of the Gas Components Identified with ASTE

Our ASTE mapping observations of the L1551 NE region have revealed three distinct gas components; *i.e.*, ENV, RED1, and RED2. ENV is the component of the protostellar envelope surrounding the protostellar binary system L1551 NE, and exhibits the dispersing gas motion as discussed above. RED1 and 2 are most likely the redshifted outflow components driven from L1551 IRS 5, which are interacting with ENV.

To discuss the interaction between ENV and RED1 and 2 quantitatively, physical parameters of these components were estimated as follows. First, the moment 0 map of each component was made in the relevant tracers and the velocity ranges listed in Table 2. As shown above, ENV is most clearly identified in the  $\text{C}^{18}\text{O}$  (3–2) emission, and RED2 in the  $^{13}\text{CO}$  (3–2) emission. We adopt the CS (7–6) emission to deduce the physical condition of RED1, because in the CS emission RED1 can be identified as a distinct gas component most easily, and the submillimeter CS emission must trace higher-temperature gas associated with outflows. We also note that it is not straightforward to separate RED2 in the 3-dimensional space from the other lower-velocity components. We here identified RED2 as the  $^{13}\text{CO}$  emission component in the highest redshifted velocity range of  $9.47 - 12.53 \text{ km s}^{-1}$ , since in this

velocity range RED2 is a distinct, highest redshifted component seen primarily in the  $^{13}\text{CO}$  emission. After making the moment 0 maps of these distinct components, two-dimensional Gaussian fittings to the moment 0 maps were performed to derive the central positions, beam-deconvolved sizes along the major and minor axes, and the total flux. For ENV a single two-dimensional Gaussian fitting to the moment 0 map did not provide a satisfactory fit. Thus, for ENV two-component, two-dimensional Gaussian fitting was performed, and the position was defined as the peak position of the central Gaussian component, while the size was defined as the size of the outer Gaussian component. The line widths of these components ( $\equiv \Delta v$ ) were derived from the FWHM values of the relevant spectra toward the central positions. Projected flow velocities of RED1 and RED2,  $v_{flow}$ , were defined as the mean velocity at the center of the components with respect to the velocity of ENV ( $= 6.7 \text{ km s}^{-1}$ ).

Masses of the components ( $\equiv M_{LTE}$ ) were derived from the total fluxes, on the assumption of the LTE condition, optically-thin emission, and the molecular abundances of  $X_{C^{18}O} = 1.7 \times 10^{-7}$  (Crapsi et al. 2004),  $X_{^{13}CO}/X_{C^{18}O} = 7.7$  (Wilson & Rood 1994), and  $X_{CS} = 6.8 \times 10^{-10}$  (Jørgensen et al. 2004). Since the peak brightness temperature ( $\equiv T_B$ ) of the  $C^{18}O$  emission toward the protobinary position exceeds  $>3.4 \text{ K}$ , the excitation temperature ( $\equiv T_{ex}$ ) must exceed  $\gtrsim 9.0 \text{ K}$  as  $J_\nu(T_{ex}) - J_\nu(T_{bg})$  must be higher than  $T_B$ . On the other hand, to excite the submillimeter CS (7–6) emission a gas temperature as high as  $\sim 60 \text{ K}$  is required (Takakuwa et al. 2007a; Takakuwa & Kamazaki 2011). Thus,  $T_{ex} = 10 - 60 \text{ K}$  is assumed as a probable range of  $T_{ex}$ . Virial masses of the components ( $\equiv M_{vir}$ ) were derived as;

$$M_{vir} = \frac{5DC_{eff}^2}{2G}, \quad (4)$$

where

$$C_{eff}^2 = \frac{\Delta v^2}{8 \ln 2}. \quad (5)$$

In the above expressions  $D$  denotes the geometrical mean of the sizes along the major and minor axes of the components, and  $C_{eff}$  the effective sound speed of gas. The isotropic velocity dispersion inside the components is assumed. For RED1 and 2, the sizes ( $\sim 4000 \text{ AU}$ ) are as small as the beam size ( $\sim 3200 \text{ AU}$ ), and thus the line widths derived from the central spectra represent the average velocity dispersions. For ENV, there is no discernible spatial variation of the  $C^{18}O$  line width as shown in the P-V diagrams (Figures 7, 8), except for that arising from the central disk. Thus, the assumption of the isotropic velocity dispersion inside these components is probably valid.

Momenta ( $\equiv p$ ), internal gas energies ( $\equiv E_{int}$ ), and kinetic energies ( $\equiv E_{kin}$ ) of the

components were derived as;

$$p^{RED1,2} = M_{LTE} v_{flow}, \quad (6a)$$

$$p^{ENV} = M_{LTE} v_{disp}, \quad (6b)$$

$$E_{int} = \frac{3}{2} M_{LTE} C_{eff}^2, \quad (7)$$

$$E_{kin}^{RED1,2} = \frac{1}{2} M_{LTE} v_{flow}^2, \quad (8a)$$

$$E_{kin}^{ENV} = \frac{1}{2} M_{LTE} v_{disp}^2. \quad (8b)$$

Table 2 summarizes these derived physical parameters. The size ( $\sim 20000$  AU) and LTE mass ( $\sim 1-3 M_{\odot}$ ) of ENV are typical of protostellar envelopes (André et al. 2000; Myers et al. 2000; Takakuwa et al. 2003). The virial mass of ENV is comparable to or slightly larger than the LTE mass plus the central protobinary mass. From the comparison between the virial and LTE masses it is not straightforward to ascertain whether ENV is gravitationally bound or not. On the other hand, the identification of the dispersing gas motion in ENV implies that ENV is gravitationally unbound. The outflow components of RED1 and 2 are characterized with their compact sizes ( $\lesssim 4000$  AU) and wide line widths ( $\sim 1-2$  km s $^{-1}$ ). The LTE masses of the outflow components are likely lower than the corresponding virial masses, although for RED1 only the upper limit of the virial mass is obtained. These results indicate that RED1 and 2 are not gravitationally-bound gas condensations, consistent with our interpretation that RED1 and 2 are outflowing gas components driven from L1551 IRS 5. The summed flow momentum of RED1 and 2 is comparable to that of the momentum of the dispersing motion in ENV. Furthermore, the net internal+kinetic energy of these outflow components is also comparable to the internal+kinetic gas energy of ENV. These results imply that RED1 and 2 can exert significant dynamical impacts on ENV, and can induce the observed dispersing gas motion of ENV through the interactions.

## 5. Discussion

### 5.1. Dispersing Envelope around the Circumbinary Disk in L1551 NE

Our new ASTE observations and combining the ASTE data with our previous SMA data in L1551 NE have revealed that the protostellar envelope around the Keplerian CBD is

being dispersed. The dispersing envelope does not show any rotating gas motion in contrast with the Keplerian rotation in the CBD, and the centroid velocity of the envelope is  $\sim 0.2$  km s $^{-1}$  blueshifted with respect to that of CBD. These results indicate that the protostellar envelope is kinematically distinct from the central CBD. The outflow components from L1551 IRS 5, as seen most prominently in the submillimeter CS (7–6) line (RED1) and the high-velocity redshifted  $^{13}\text{CO}$  (3–2) line (RED2), appear to collide and interact with the protostellar envelope. The net momentum, and kinetic and internal energy of these outflow components are comparable to those of ENV, suggesting that the outflow collisions can enforce significant dynamical impacts on the envelope. A natural interpretation of these results is that the protostellar envelope in L1551 NE is being disrupted through the interaction with the outflows driven from L1551 IRS 5. Figure 14 (bottom) shows a schematic, inferred configuration of the L1551 region viewed from the north, in parallel with the SCUBA 850  $\mu\text{m}$  dust-continuum image (Moriarty-Schieven et al. 2006) as a representative projected image onto the sky plane (top). In the SCUBA image a torus-like continuum feature connecting the envelopes around L1551 IRS 5 and NE is seen as delineated with a dashed green curve. This feature is drawn schematically in the bottom as the northernmost feature. Since the envelope around L1551 NE is being collided with the redshifted outflow components driven from L1551 IRS 5 (RED1 and 2), the location of L1551 NE must be backward with respect to the location of L1551 IRS 5 along the line of sight. As already described the western side of the flattened envelope around L1551 NE is far-side and the eastern side near-side. Thus the blueshifted emission to the east and the redshifted emission to the west are interpreted as the dispersing gas motion in the flattened envelope.

Our ASTE single-dish observations of the  $^{13}\text{CO}$  (3–2),  $\text{C}^{18}\text{O}$  (3–2), CS (7–6), and SO (7 $_8$ –6 $_7$ ) lines, as well as SMA and ALMA observations of the  $^{13}\text{CO}$  (3–2) and  $\text{C}^{18}\text{O}$  (3–2) lines (Takakuwa et al. 2012; Takakuwa et al. 2013; Takakuwa et al. 2014), do not find any evidence for molecular outflows driven from L1551 NE itself. On the other hand, previous NIR observations of L1551 NE found collimated [Fe II] jets driven from Source A as well as a reflection nebula with its apex close to the position of Source B (Reipurth et al. 2000; Hayashi & Pyo 2009). Molecular outflows driven from L1551 NE have also been reported in the  $^{12}\text{CO}$  (3–2; 2–1; 1–0) lines (Moriarty-Schieven et al. 1995; Moriarty-Schieven et al. 2006; Stojimirović et al. 2006), although it is not straightforward to disentangle the outflows from L1551 IRS 5 and NE because of the close overlaps of the two outflows. Our ASTE observations show that interactions with the powerful L1551 IRS 5 outflows have greater impact on the disruption of the envelope than the outflow driven from L1551 NE itself. This is in contrast with previous findings of interactions between protostellar envelopes and outflows or stellar winds driven from the sources embedded in the envelopes (Kitamura et al. 1996; Momose et al. 1996; Fuente et al. 2002; Takakuwa et al. 2003; Arce & Sargent 2006; Takahashi et al. 2006).

Yokogawa et al. (2003) have suggested that the interactions with the outflows driven from L1551 IRS 5 triggered the star formation in L1551 NE. We consider, however, that the formation of the protostellar binary system L1551 NE has initiated before the arrival of the IRS 5 outflows, because at present the protostellar envelope is kinematically distinct and thus physically detached from the CBD and the protostellar binary system. The similar binary masses ( $\sim 0.8 M_{\odot}$  in L1551 NE and  $\sim 0.5 M_{\odot}$  in IRS 5), envelope masses ( $\sim 1 M_{\odot}$ ), and the bolometric temperatures ( $T_{bol} \sim 90$  K) indicate that both L1551 IRS 5 and NE were born at a similar age. After their birth both L1551 NE and IRS 5 grow simultaneously. The angular separation between L1551 IRS 5 and NE is  $\sim 2''.5$ , and assuming the transverse velocity of the outflows driven from L1551 IRS 5 is  $\sim 10$  km s $^{-1}$  (Moriarty-Schieven et al. 2006; Stojimirović et al. 2006; Wu et al. 2009), the transverse time for the IRS 5 outflow to reach the L1551 NE location is  $\sim 10^4$  yr. This time scale is approximately consistent with the estimated age of L1551 NE of  $0.6\text{--}5.0 \times 10^4$  yr (Motte & André 2001). After the outflows from L1551 IRS 5 have arrived at the protostellar envelope around L1551 NE, the outflows start disrupting the envelope through the interactions. The possible infalling motion in the inner envelope found with the SMA may be a remnant gas motion before the initiation of the interactions with the IRS 5 outflows. Such a remnant infalling gas motion embedded in the dispersing envelope has also been identified in a T-Tauri star DG Tauri (Kitamura et al. 1996).

The envelope dispersion via the interactions with the IRS 5 outflows will impact the final fates of the protostellar binary system of L1551 NE significantly, as will be discussed in the next subsection.

## 5.2. Implication of Envelope Dispersion for Binary Growth

Binary stars with the primary masses comparable to that of the Sun show a wide range of the binary mass ratios, and the distribution of the mass ratio ( $\equiv q$ ) is essentially flat from  $q \sim 0.1$  to 1 (Raghavan et al. 2010; Goodwin 2013). Physical mechanisms to reproduce such a wide range of binary mass ratios have been controversial, and gas accretion in the CBDs onto the protostellar binaries has been discussed as a mechanism to set the final binary mass ratios. Smoothed particle hydrodynamic (SPH) simulations of circumbinary accretion show that the majority of materials accrete onto the secondary, because the secondary orbits further from the center of mass of the binary and thus sweeps more materials in the CBD than the primary (Bate 1997; Bate & Bonnell 1997; Bate 2000). Our 3-D adaptive mesh refinement (AMR) hydrodynamic simulation (Matsumoto 2007) to reproduce the ALMA results of the CBD in L1551 NE also shows that the secondary (Source B) accretes more



than the primary (Source A) (Takakuwa et al. 2014). On the other hand, high-resolution grid-based simulations by Ochi et al. (2005) and Hanawa et al. (2010) show that primaries accrete more than secondaries. Latest SPH simulations demonstrate that flows from the secondary to the primary within the Roche lobes are a sensitive function of gas temperatures, and in the case of the high temperature the primary accretes more than the secondary, and vice versa (Young et al. 2015).

Our ASTE observations of an archetypal protostellar binary L1551 NE imply that dispersion of protostellar envelopes, which replenish CBDs with fresh materials, also needs to be taken into account as a physical mechanism to set the binary masses and the ratios. The present masses of Sources A and B in L1551 NE are estimated to be  $\sim 0.67 M_{\odot}$  and  $\sim 0.13 M_{\odot}$ , respectively, and the mass of the CBD  $\sim 0.026 M_{\odot}$  (Takakuwa et al. 2012). The mass of the possible infalling component around the CBD is even smaller ( $\sim 0.0023 M_{\odot}$ ) (Takakuwa et al. 2013). Thus, even if all the amount of the material in the CBD plus the infalling component is accreted onto Source B, the mass ratio does not change much (from 0.19 to 0.24). Replenishment of the material to the CBD from the surrounding envelope is required to significantly change the mass and the mass ratio of the protostellar binary system. Our ASTE observations show that the envelope is being dispersed, however, and that further replenishment of materials from the envelope to the CBD will not be expected. Therefore, even though L1551 NE is a Class I protostellar binary associated with the CBD and the protostellar envelope, the mass and the mass ratio have been already close to the final values. Physical processes before the start of the envelope dispersion through the interaction with the outflow driven from L1551 IRS 5, such as the fragmentation of the initial pseudo-disk and subsequent accretion from the CBD and the envelope, must be responsible to set the mass and mass ratio of the binary system.

Our ASTE observations of L1551 NE indicate that dispersion of natal envelopes surrounding the protostellar binary systems is one of the key physical phenomena to stop the growth of the binary and to determine the final masses and the mass ratios of the binary. As described in the last subsection, interactions between protostellar envelopes and outflows, which causes the envelope dissipation, are ubiquitous. Systematic studies of envelope dispersion surrounding the protostellar binaries with various masses and mass ratios will be intriguing to understand the physical mechanism to set the final binary mass ratios and the origin of the wide range of the binary mass ratios.

## 6. Summary

We have conducted single-dish mapping observations of dense gas around an archetypal protostellar binary L1551 NE in the  $\text{C}^{18}\text{O}$  ( $J=3-2$ ),  $^{13}\text{CO}$  ( $J=3-2$ ), CS ( $J=7-6$ ), and the SO ( $J_N=7_8-6_7$ ) lines with ASTE. We have also combined the ASTE mapping data in the  $\text{C}^{18}\text{O}$  line with the interferometric data taken with the SMA. The main results are summarized below:

1. All the four molecular lines are detected toward the protostellar position, with multiple and/or non-Gaussian spectral shapes. In particular, the  $\text{C}^{18}\text{O}$  spectrum consists of a narrow ( $\Delta v \sim 0.7 \text{ km s}^{-1}$ ) component with a central velocity of  $V_{\text{LSR}} \sim 6.7 \text{ km s}^{-1}$  and a wide ( $\Delta v \sim 2.2 \text{ km s}^{-1}$ ) component with a central velocity of  $V_{\text{LSR}} \sim 6.9 \text{ km s}^{-1}$ . The wide component originates from the compact circumbinary disk (CBD), while the narrow component from the extended protostellar envelope.
2. The  $\text{C}^{18}\text{O}$  map in L1551 NE primarily traces a  $\sim 20000$ -AU scale protostellar envelope (ENV), elongated along the northwest to southeast direction, approximately parallel to the major axis of the central CBD. Velocity channel maps of the  $\text{C}^{18}\text{O}$  line show that the blueshifted ( $V_{\text{LSR}} \sim 6.2\text{--}6.7 \text{ km s}^{-1}$ ) emission is located to the northeast while the redshifted emission ( $V_{\text{LSR}} \sim 6.7\text{--}8.0 \text{ km s}^{-1}$ ) to the southwest; *i.e.*, a velocity gradient of ENV along the minor axis, while there is no detectable velocity gradient along the major axis. The observed velocity gradient in ENV can be interpreted as a dispersing gas motion. Velocity channel maps of the high-velocity redshifted ( $V_{\text{LSR}} \gtrsim 8.0 \text{ km s}^{-1}$ )  $^{13}\text{CO}$  emission show two  $\lesssim 4000$ -AU scale redshifted components to the  $\sim 40''$  southwest of the central protostar (RED1) and  $\sim 20''$  west (RED2). The submillimeter CS ( $7-6$ ) emission selectively traces RED1, suggesting high-temperature in this high-velocity component. Both RED1 and RED2 exhibit similar velocity gradients such that the velocities become closer to the systemic velocity of ENV as the positions become closer to that of ENV. These high-velocity redshifted components most likely trace the outflow components driven from the neighboring protostellar source, L1551 IRS 5, which are colliding with ENV surrounding L1551 NE.
3. The combined ASTE+SMA map in the  $\text{C}^{18}\text{O}$  emission shows that the  $r \sim 300$  AU scale CBD and  $r \sim 700$  AU scale infalling component found in our previous SMA observations are surrounded by ENV with a slightly blueshifted velocity ( $\sim 0.2 \text{ km s}^{-1}$ ). ENV does not show any rotational motion but dispersing gas motion with an outward velocity of  $\sim 0.3 \text{ km s}^{-1}$  in contrast to the inner gas components. These results indicate that ENV is kinematically distinct from the inner gas components.

4. The net momentum, kinetic and internal energies of the redshifted outflow components driven from L1551 IRS 5 are comparable to those of ENV, suggesting that the outflow collisions can enforce significant dynamical impacts on ENV. Thus, the dispersing motion in ENV is likely caused by the interactions with the outflows driven from L1551 IRS 5.
5. Since ENV is being dispersed and the inner gas components do not have sufficient materials to alter the mass and mass ratio of the protostellar binary of L1551 NE, the current mass ( $\sim 0.8 M_{\odot}$ ) and the mass ratio ( $\sim 0.19$ ) are close to the final values, even though L1551 NE is a young Class I protostellar binary. Our ASTE+SMA observations of L1551 NE suggest that dispersion of natal protostellar envelopes which can replenish the CBDs with new materials is one of the important physical mechanisms to set the final binary mass ratios. The interactions with the outflows from L1551 IRS 5 are unlikely to trigger the binary formation in L1551 NE as suggested by previous studies, but suppress the further growth of the protostellar binary system.

We would like to thank T. Matsumoto, T. Hanawa, J. Lim, N. Ohashi, and P. T. P. Ho for their fruitful discussions. We are grateful to S. Ohashi for his support during our ASTE observations. S.T. acknowledges a grant from the Ministry of Science and Technology (MOST) of Taiwan (MOST 102-2119-M-001-012-MY3) in support of this work.

## REFERENCES

- André, P., Ward-Thompson, D., & Barsony, M. 2000, in *Protostars and Planets IV*, ed. Mannings, V., Boss, A. P., & Russell, S. S. (Tucson: Univ. Arizona Press), 59
- Arce, H. G. & Sargent, A. I. 2006, *ApJ*, 646, 1070
- Bate, M. R. 1997, *MNRAS*, 285, 16
- Bate, M. R., & Bonnell, I. A. 1997, *MNRAS*, 285, 33
- Bate, M. R. 2000, *MNRAS*, 314, 33
- Chen, X., Arce, H. G., Zhang, Q. *et al.* 2013, *ApJ*, 768, 110
- Chou, T.-L., Takakuwa, S., Yen, H.-W., Ohashi, N., & Ho, P. T. P. 2014, *ApJ*, 796, 70
- Crapsi, A., Caselli, P., Walmsley, C. M., *et al.* 2004, *A&A*, 420, 957

- Dutrey, A., Di Folco, E., Guilloteau, S., *et al.* 2014, *Nature*, 514, 600
- Froebrich, D. 2005, *ApJS*, 156, 169
- Fuente, A., Martín-Pintado, J., Bachiller, R., Rodríguez-Franco, A., & Palla, F. 2002, *A&A*, 387, 977
- Fuller, G. A., & Ladd, E. F. 2002, *ApJ*, 573, 699
- Goodwin, S. P. 2013, *MNRAS*, 430, L6
- Hanawa, T., Ochi, Y., & Ando, K. 2010, *ApJ*, 708, 485
- Hayashi, M. & Pyo, T.-S. 2009, *ApJ*, 694, 582
- Jørgensen, J. K., Schöier, F. L., & van Dishoeck, E. F. 2004, *A&A*, 416, 603
- Kamazaki, T., Ezawa, H., Tatematsu, K., *et al.* 2005, *Astronomical Data Analysis Software and Systems XIV*, ASP Conf. Ser., 347, ed. P. Shopbell, M. Britton, & R. Ebert, (San Francisco: ASP), 533
- Kitamura, Y., Kawabe, R., & Saito, M. 1996, *ApJ*, 457, 277
- Kohno, K. 2005, *The Cool Universe: Observing Cosmic Dawn*, ASP Conf. Ser. 344, ed. C. Lidman & D. Alloin, (San Francisco: ASP), 242
- Matsumoto, T. 2007, *PASJ*, 59, 905
- Momose, M., Ohashi, N., Kawabe, R., Hayashi, M., & Nakano, T. 1996, *ApJ*, 470, 1001
- Momose, M., Ohashi, N., Kawabe, R., Nakano, T., & Hayashi, M. 1998, *ApJ*, 504, 314
- Moriarty-Schieven, G. H., Butner, H. M. & Wannier, P. G. 1995, *ApJ*, 445, L55
- Moriarty-Schieven, G. H., Johnstone, D., Bally, J., & Jenness, T. 2006, *ApJ*, 645, 357
- Motte, F., & André, P. 2001, *A&A*, 365, 440
- Myers, P. C., Evans, N. J., II & Ohashi, N. 2000, in *Protostars and Planets IV*, ed. Mannings, V., Boss, A. P., & Russell, S. S. (Tucson: Univ. Arizona Press), 217
- Ochi, Y., Sugimoto, K., & Hanawa, T. 2005, *ApJ*, 623, 922
- Plambeck, R. L., & Snell, R. L. 1995, *ApJ*, 446, 234
- Raghavan, D., McAlister, H. A., Henry, T. J. *et al.* 2010, *ApJS*, 190, 1

- Reipurth, B., Yu, K. C., Heathcote, S., Bally, J., & Rodríguez, L. F. 2000, *AJ*, 120, 1449
- Reipurth, B., Rodríguez, L. F., Anglada, G., & Bally, J. 2002, *AJ*, 124, 1045
- Reipurth, B., Clarke, C. J., Boss, A. P. *et al.* 2014, *Protostars and Planets VI*, 267
- Saito, M., Kawabe, R., Kitamura, Y., & Sunada, K. 2001, *ApJ*, 547, 840
- Schilke, P., Groesbeck, T. D., Blake, G. A., & Phillips, T. G. 1997, *ApJS*, 108, 301
- Stojimirović, I., Narayanan, G., Snell, R. L., & Bally, J. 2006, *ApJ*, 649, 280
- Takahashi, S., Saito, M., Takakuwa, S., & Kawabe, R. 2006, *ApJ*, 651, 933
- Takakuwa, S., Ohashi, N., & Hirano, N. 2003, *ApJ*, 590, 932
- Takakuwa, S., Ohashi, N., Ho, P. T. P., *et al.* 2004, *ApJ*, 616, L15
- Takakuwa, S., Kamazaki, T., Saito, M., Yamaguchi, N., & Kohno, K. 2007, *PASJ*, 59, 1
- Takakuwa, S., Ohashi, N., Bourke, T. L., *et al.* 2007, *ApJ*, 662, 431
- Takakuwa, S., & Kamazaki, T. 2011, *PASJ*, 63, 921
- Takakuwa, S., Saito, M., Lim, J., *et al.* 2012, *ApJ*, 754, 52
- Takakuwa, S., Saito, M., Lim, J., & Saigo, K. 2013, *ApJ*, 776, 51
- Takakuwa, S., Saito, M., Saigo, K., *et al.* 2014, *ApJ*, 796, 1
- Tang, Y.-W., Dutrey, A., Guilloteau, S., *et al.* 2014, *ApJ*, 793, 10
- Tobin, J. J., Chandler, C. J., Wilner, D. J., *et al.* 2013, *ApJ*, 779, 93
- Wilson, T. L., & Rood, R. 1994, *ARA&A*, 32, 191
- Wu, P.-F., Takakuwa, S., & Lim, J. 2009, *ApJ*, 698, 184
- Yokogawa, S., Kitamura, Y., Momose, M., & Kawabe, R. 2003, *ApJ*, 595, 266
- Young, M. D., Baird, J. T., & Clarke, C. J. 2015, *MNRAS*, 447, 2907

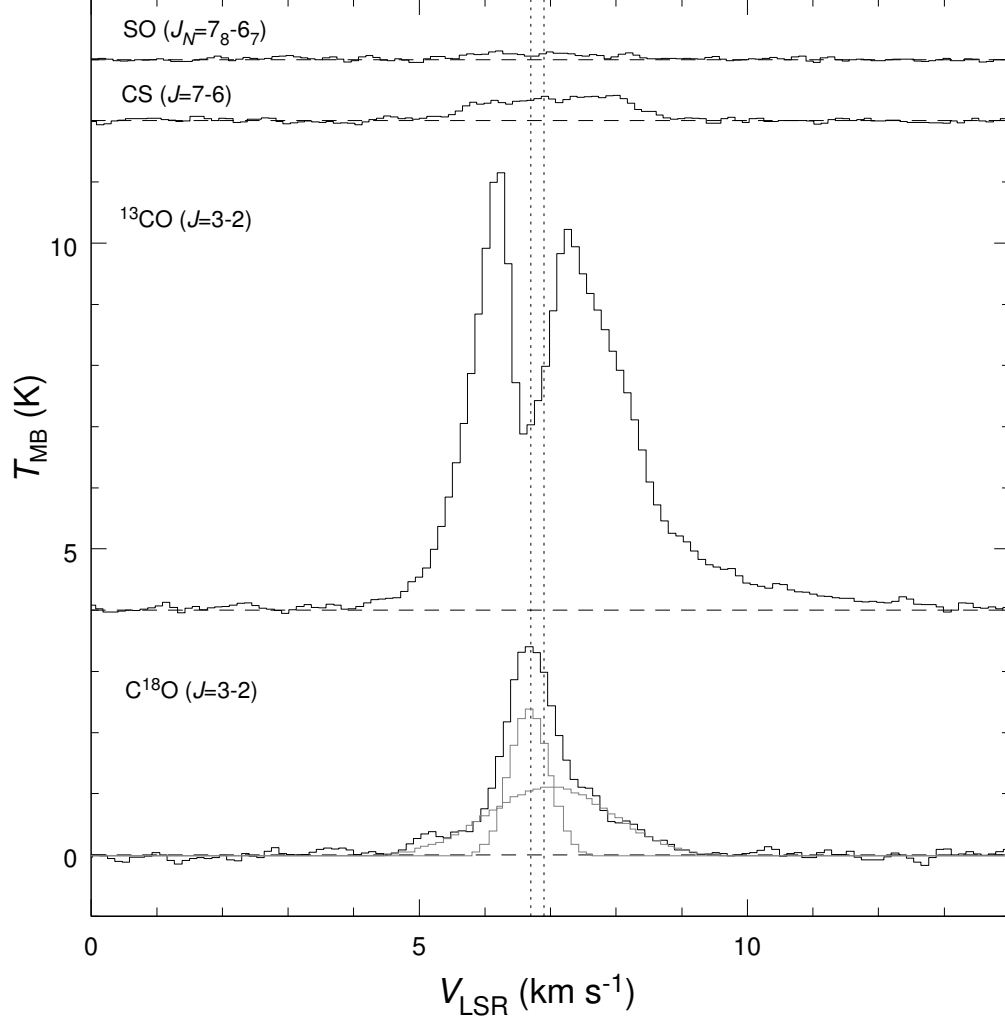


Fig. 1.— ASTE spectra toward the central position of L1551 NE. Light lines at the bottom show the results of the two-component Gaussian fitting to the observed  $\text{C}^{18}\text{O}$  (3–2) spectrum. The vertical dashed lines denote the centroid velocities of the envelope ( $V_{\text{LSR}} = 6.7 \text{ km s}^{-1}$ ) and the central circumbinary disk ( $V_{\text{LSR}} = 6.9 \text{ km s}^{-1}$ ).

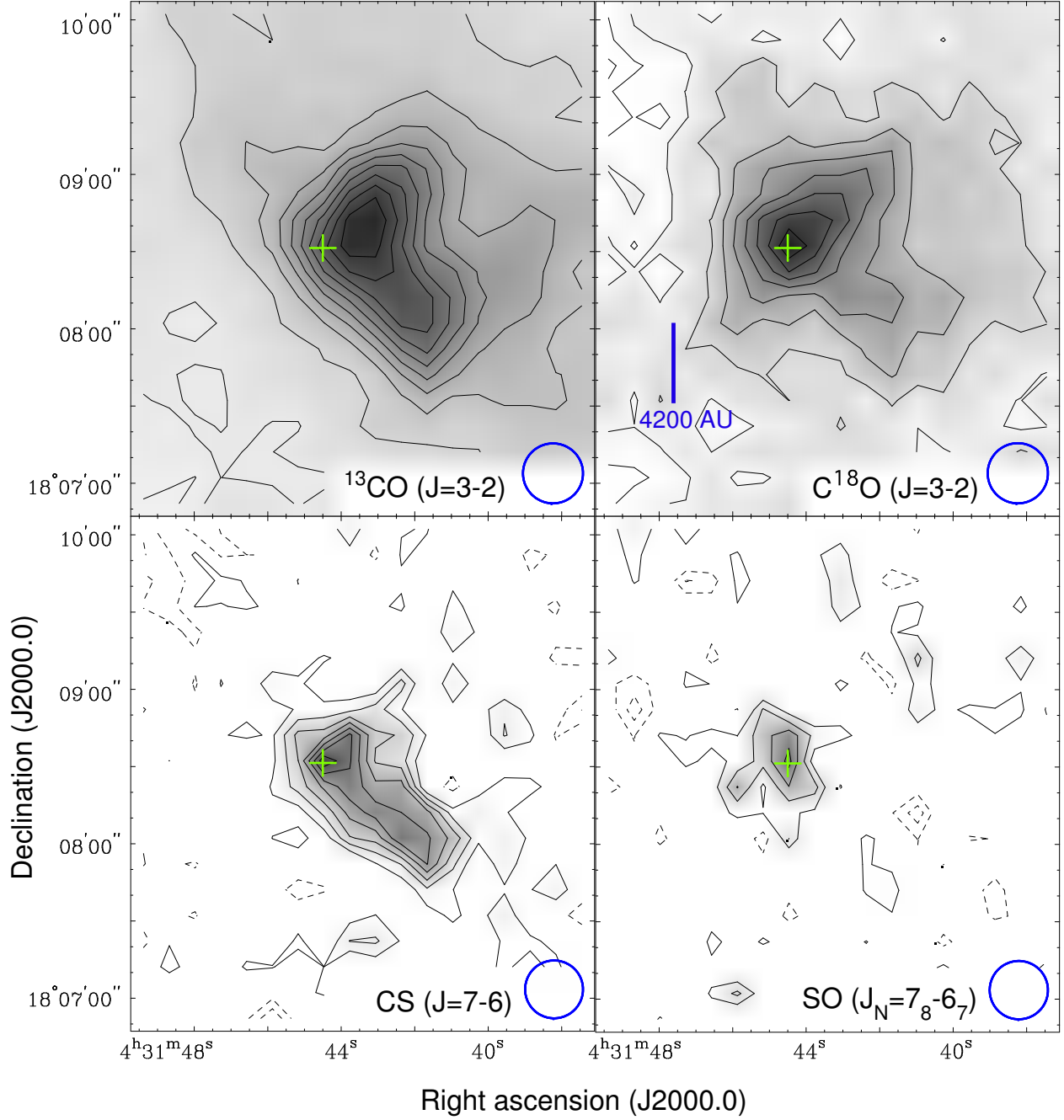


Fig. 2.— ASTE total integrated intensity maps of the observed lines as labeled. Crosses show the position of L1551 NE. Integrated velocity ranges are  $4.48 - 12.53 \text{ km s}^{-1}$ ,  $5.31 - 9.86 \text{ km s}^{-1}$ ,  $5.63 - 9.13 \text{ km s}^{-1}$ , and  $5.69 - 8.00 \text{ km s}^{-1}$ , for the  $^{13}\text{CO}$  (3–2),  $\text{C}^{18}\text{O}$  (3–2), CS (7–6), and the SO ( $J_N=7_8-6_7$ ) maps, respectively. Contour levels are  $15\sigma$ ,  $20\sigma$ , and then in steps of  $15\sigma$  ( $1\sigma = 0.137 \text{ K km s}^{-1}$ ) for the  $^{13}\text{CO}$  (3–2) map,  $2\sigma$ ,  $5\sigma$ , and then in steps of  $5\sigma$  ( $1\sigma = 0.130 \text{ K km s}^{-1}$ ) for the  $\text{C}^{18}\text{O}$  (3–2) map, and in steps of  $2\sigma$  for the CS (7–6) and SO ( $7_8-6_7$ ) maps ( $1\sigma = 0.0633 \text{ K km s}^{-1}$  and  $0.0517 \text{ K km s}^{-1}$  for the CS and SO maps, respectively.). Open circles at the bottom-right corners denote the ASTE beam of the relevant lines.

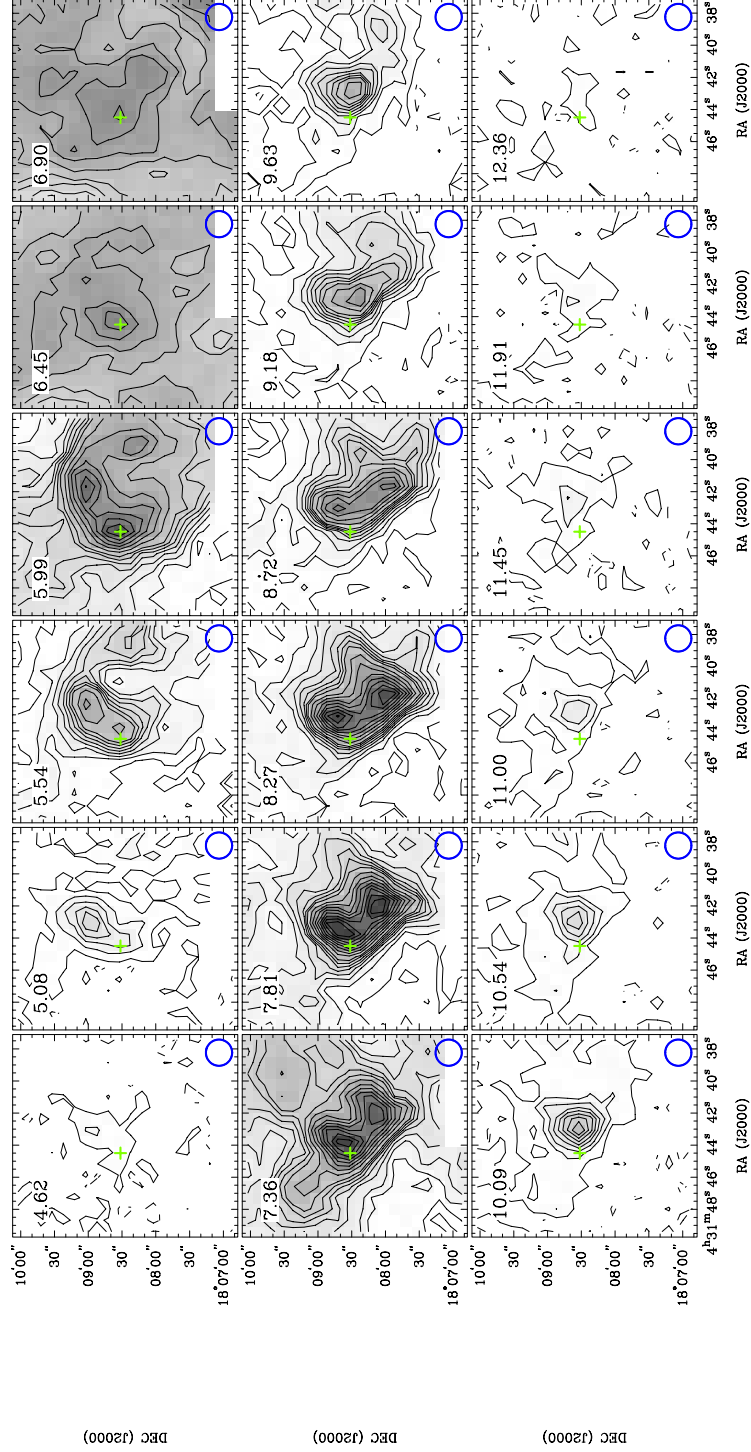


Fig. 3.— ATE velocity channel maps of the  $^{13}\text{CO}$  (3–2) line in L1551 NE at a velocity bin of  $0.455 \text{ km s}^{-1}$ . Contour levels start from  $2\sigma$  in steps of  $4\sigma$  until  $30\sigma$ , and then in steps of  $8\sigma$  ( $1\sigma = 0.0717 \text{ K}$ ). Symbols are the same as those in Figure 2.



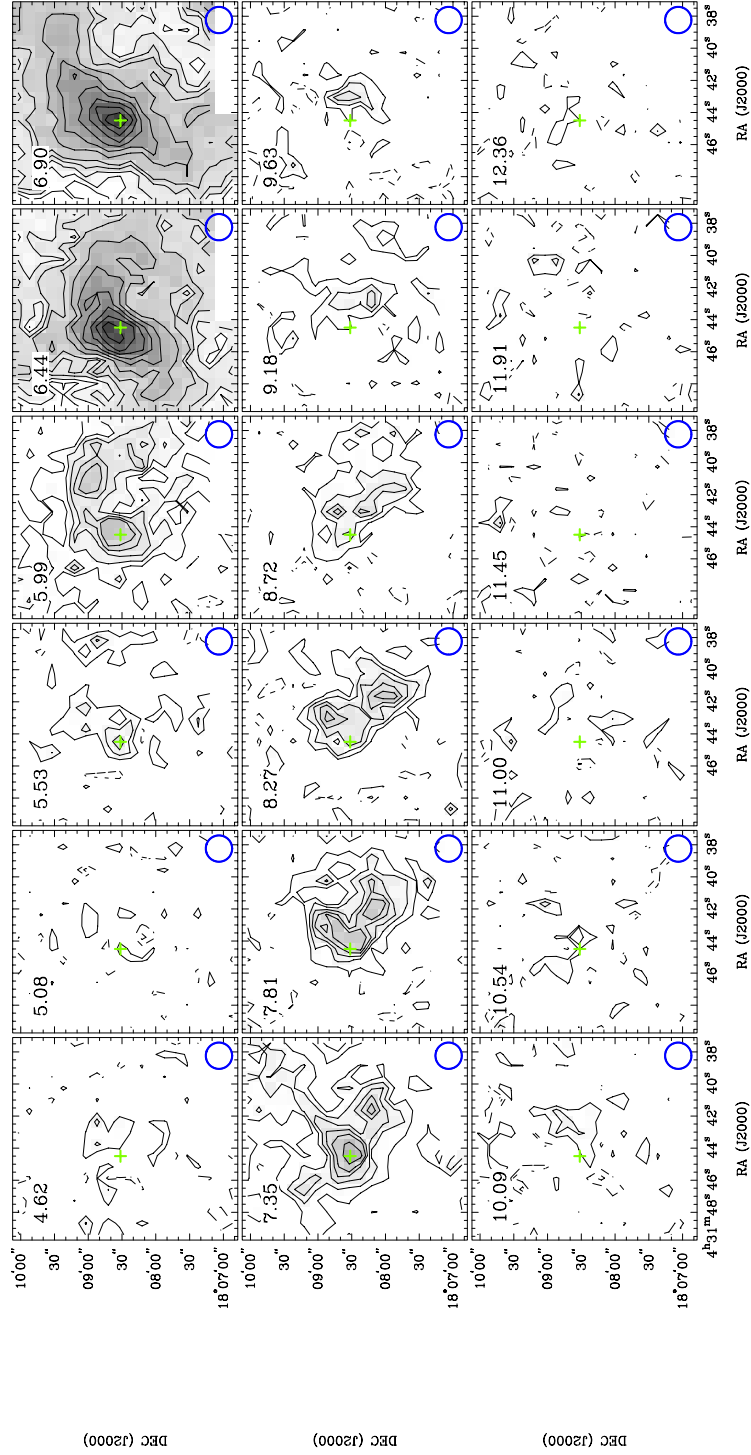


Fig. 4.— Same as Figure 3 but for the  $\text{C}^{18}\text{O}$  (3–2) line. Contour levels start from  $2\sigma$  in steps of  $2\sigma$  until  $10\sigma$ , and then in steps of  $4\sigma$  ( $1\sigma = 0.090$  K).

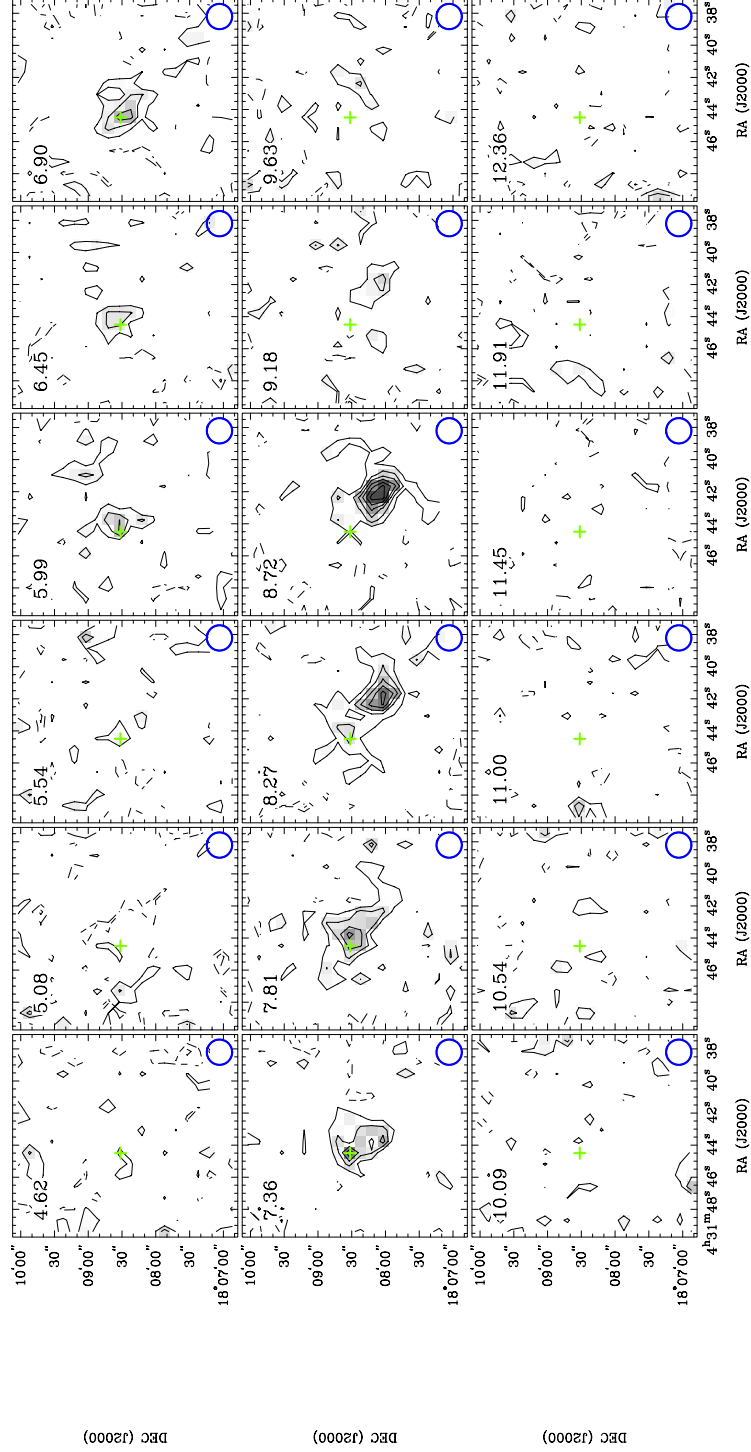


Fig. 5.— Same as Figure 3 but for the CS (7–6) line. Contour levels start from  $2\sigma$  in steps of  $2\sigma$  ( $1\sigma = 0.050$  K).

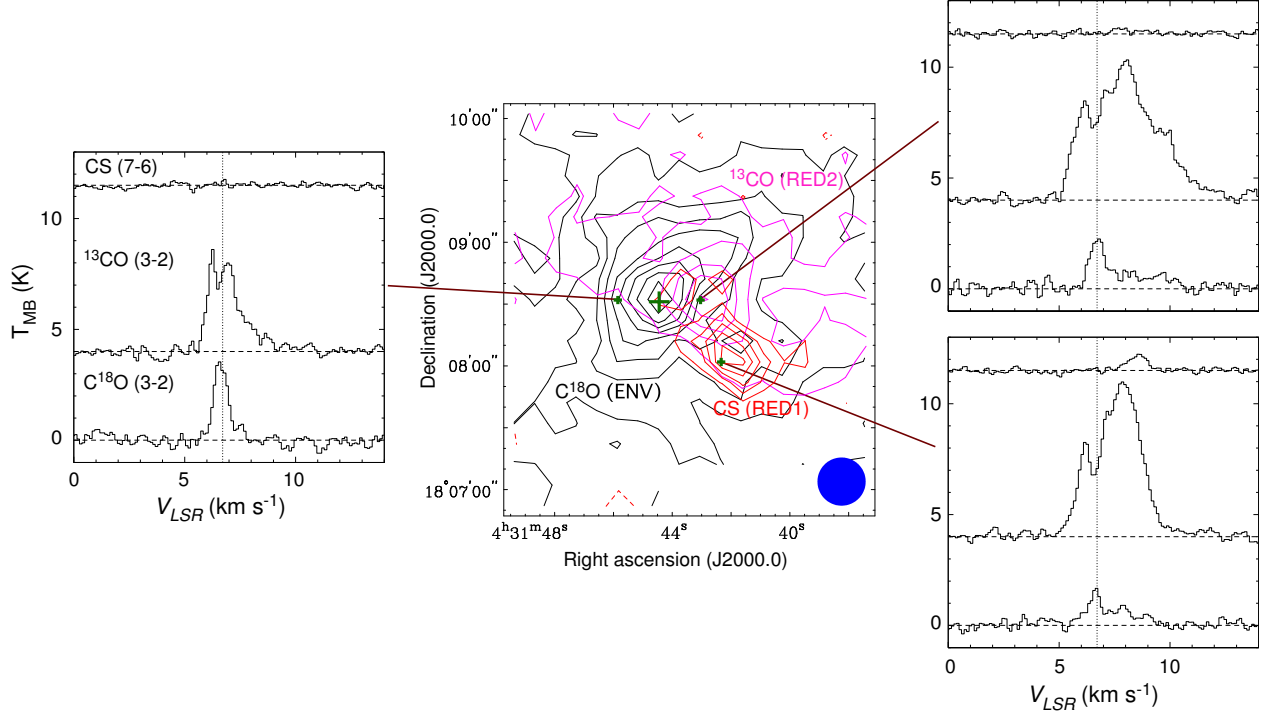


Fig. 6.— Maps of the envelope component in the  $\text{C}^{18}\text{O}$  (3–2) line (black contours), the high-velocity redshifted component in the  $^{13}\text{CO}$  (3–2) line (purple contours), and the redshifted CS (7–6) component (red contours), along with the line profiles toward the representative positions marked with crosses. Velocity ranges of the  $\text{C}^{18}\text{O}$ ,  $^{13}\text{CO}$ , and the CS maps are  $5.31 - 8.15 \text{ km s}^{-1}$ ,  $9.47 - 12.53 \text{ km s}^{-1}$ , and  $8.04 - 9.13 \text{ km s}^{-1}$ , respectively. Contour levels start from  $5\sigma$  in steps of  $5\sigma$  in the  $\text{C}^{18}\text{O}$  map ( $1\sigma = 0.036 \text{ K}$ ),  $5\sigma$  in steps of  $10\sigma$  in the  $^{13}\text{CO}$  map ( $1\sigma = 0.028 \text{ K}$ ), and  $4\sigma$  in steps of  $3\sigma$  in the CS map ( $1\sigma = 0.032 \text{ K}$ ). A large cross and a filled circle at the bottom-right corner denote the protostellar position and the ASTE beam in the  $\text{C}^{18}\text{O}$  map, respectively. Vertical dashed lines in the spectra show the systemic velocity of the envelope of  $V_{\text{LSR}} = 6.7 \text{ km s}^{-1}$ .

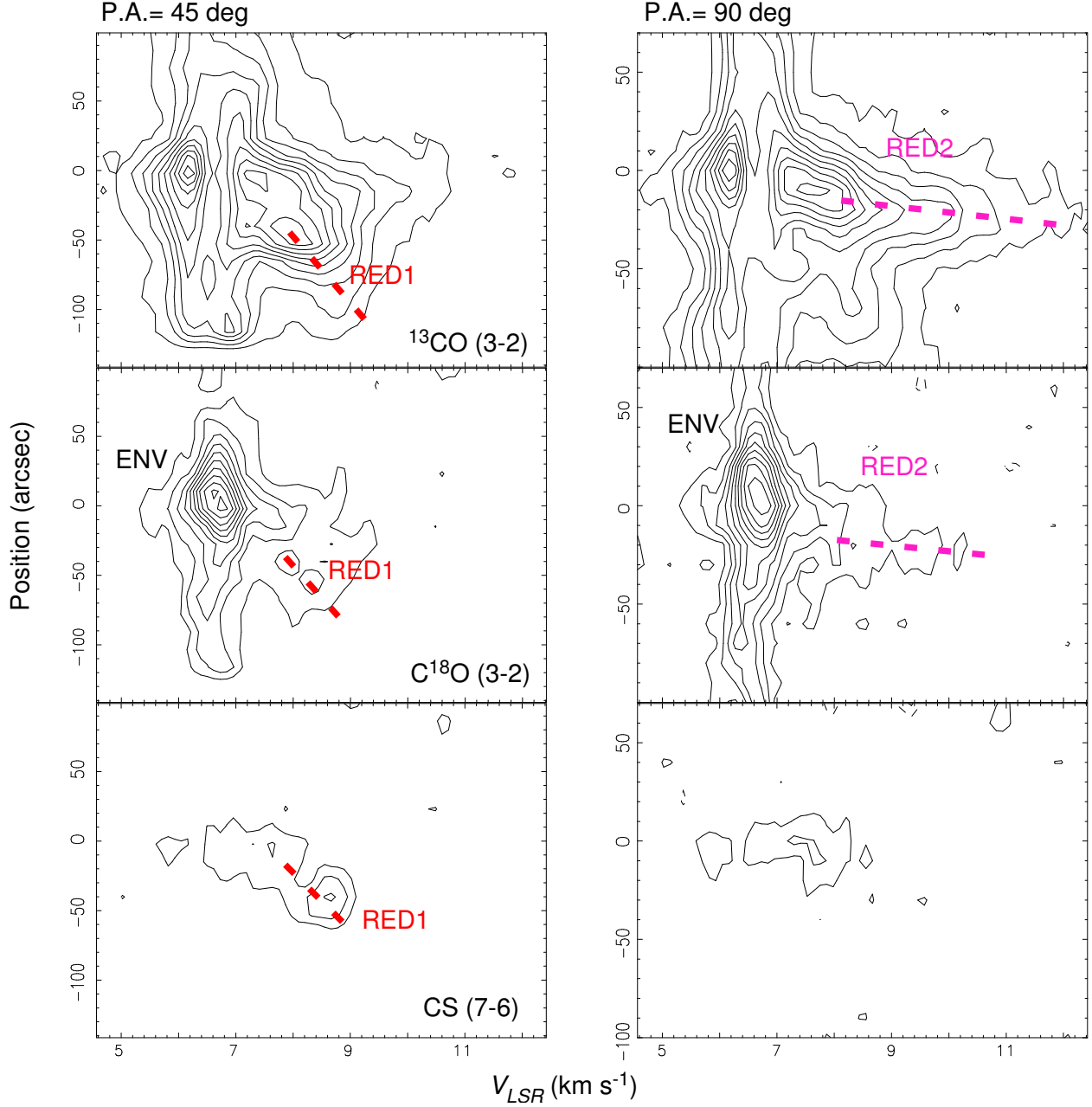


Fig. 7.— ASTE Position-Velocity (P-V) diagrams of the  $^{13}\text{CO}$  (3–2) (upper panels),  $\text{C}^{18}\text{O}$  (3–2) (middle), and the CS (7–6) lines (lower) along the cuts passing through the protostellar position at P.A. =  $45^\circ$  (left panels) and P.A. =  $90^\circ$  (right). These cut lines connect the protostellar position and the positions of RED1 and RED2 shown in Figure 6. Contour levels start from  $2.5\sigma$  in steps of  $5\sigma$  in the  $^{13}\text{CO}$  P-Vs ( $1\sigma = 0.143$  K), and in steps of  $2\sigma$  for the  $\text{C}^{18}\text{O}$  ( $1\sigma = 0.18$  K) and CS P-Vs ( $1\sigma = 0.1$  K). For direct comparison the velocity bins of the three P-Vs are aligned to be the same with the width of  $0.114$  km s $^{-1}$ . Red and purple dashed lines delineate the detected velocity gradients of RED1 and RED2, respectively.

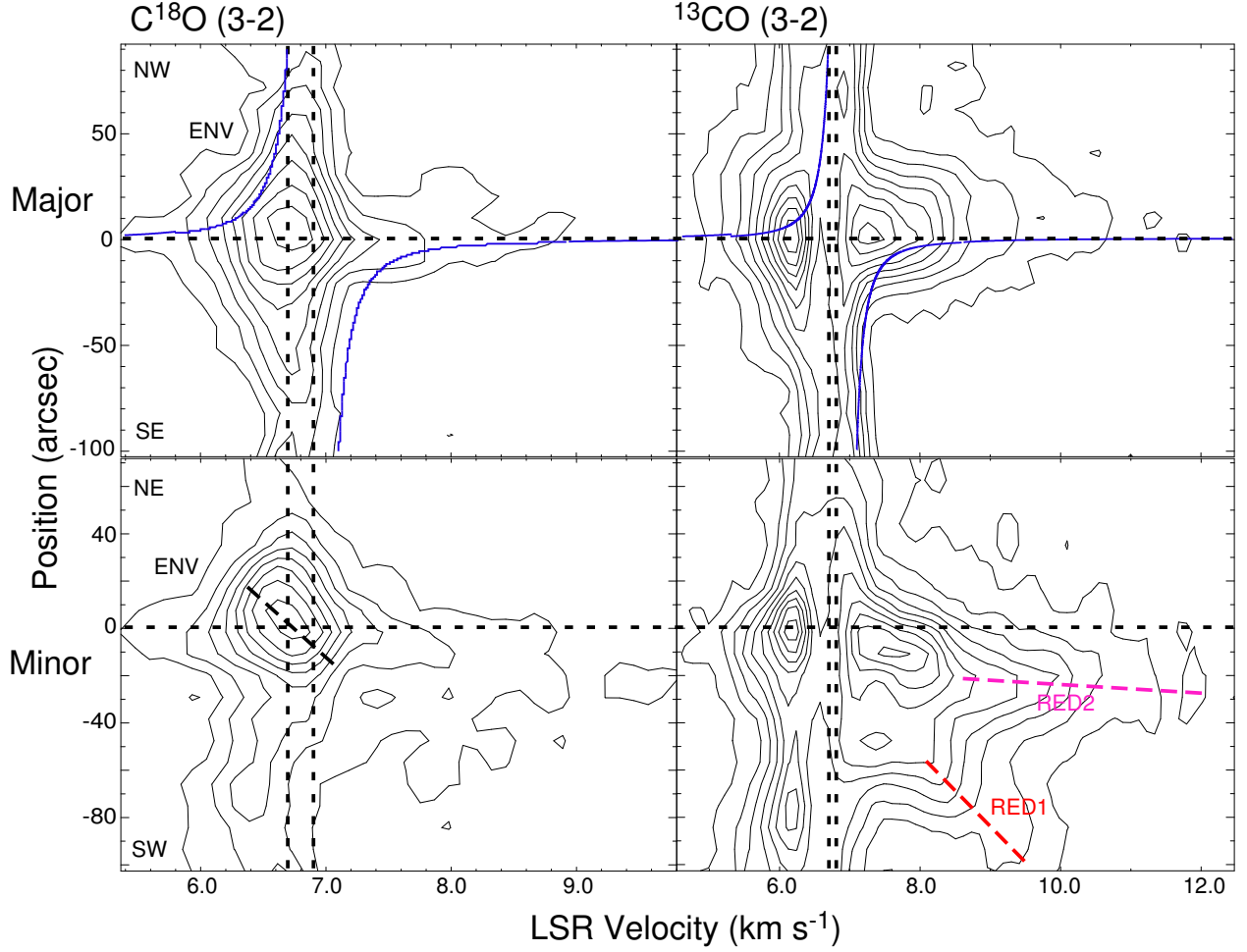


Fig. 8.— ASTE P-V diagrams of the  $\text{C}^{18}\text{O}$  (3–2) (left panels) and  $^{13}\text{CO}$  (3–2) (right) lines along the major (P.A. =  $167^\circ$ ; upper panels) and minor (P.A. =  $77^\circ$ ; lower) axes of the Keplerian CBD around L1551 NE. Contour levels are in steps of  $2.5\sigma$  for the  $\text{C}^{18}\text{O}$  P-Vs ( $1\sigma = 0.180$  K), and start from  $2.5\sigma$  in steps of  $5\sigma$  for the  $^{13}\text{CO}$  P-Vs ( $1\sigma = 0.143$  K). Horizontal dashed lines show the protostellar position, and the vertical dashed lines the centroid velocities of the extended  $\text{C}^{18}\text{O}$  envelope ( $= 6.7$  km s $^{-1}$ ) and the Keplerian CBD ( $= 6.9$  km s $^{-1}$ ). Blue curves show the rotation curve of the central Keplerian CBD. A black tilted dashed line delineates the detected velocity gradient of the envelope, and red and purple dashed lines that of RED1 and RED2, respectively.

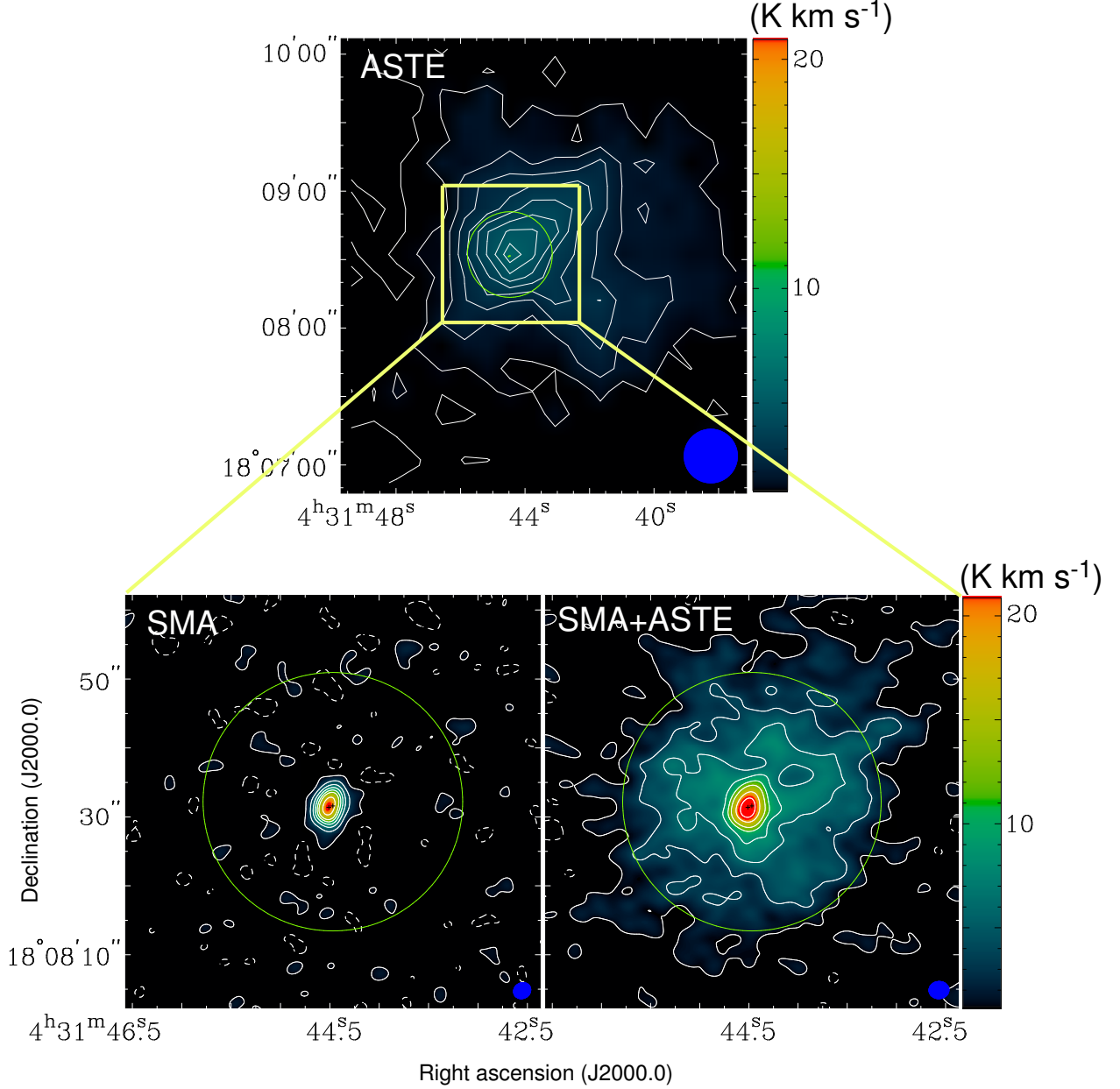


Fig. 9.— ASTE, SMA, and SMA+ASTE total integrated intensity maps of the C<sup>18</sup>O (3–2) line in L1551 NE as labeled. Integrated velocity ranges of the ASTE, SMA, and SMA+ASTE maps are 5.31 – 9.86 km s<sup>-1</sup>, 3.75 – 9.49 km s<sup>-1</sup>, and 3.94 – 9.30 km s<sup>-1</sup>, respectively. An rms noise level of the SMA+ASTE map is  $\sigma_{comb} = 0.596$  K km s<sup>-1</sup>, and the contour levels of the SMA and SMA+ASTE maps start from  $2\sigma_{comb}$  in steps of  $4\sigma_{comb}$  until  $22\sigma_{comb}$ , and then in steps of  $8\sigma_{comb}$ . Contour levels of the ASTE map are in steps of  $1\sigma_{comb}$ . Rms noise levels of the ASTE and SMA maps are  $1\sigma_{ASTE} = 0.130$  K km s<sup>-1</sup> and  $1\sigma_{SMA} = 0.379$  K km s<sup>-1</sup>, respectively. Open circles and crosses show the field of view of the SMA and the positions of the protostellar binary, respectively. Filled ellipses at the bottom-right corners denote the beam sizes ( $23''.4$  in the ASTE map,  $2''.50 \times 2''.20$ ; P.A. =  $-60^\circ.6$  in the SMA map, and  $2''.85 \times 2''.45$ ; P.A. =  $-85^\circ.3$  in the SMA+ASTE map).

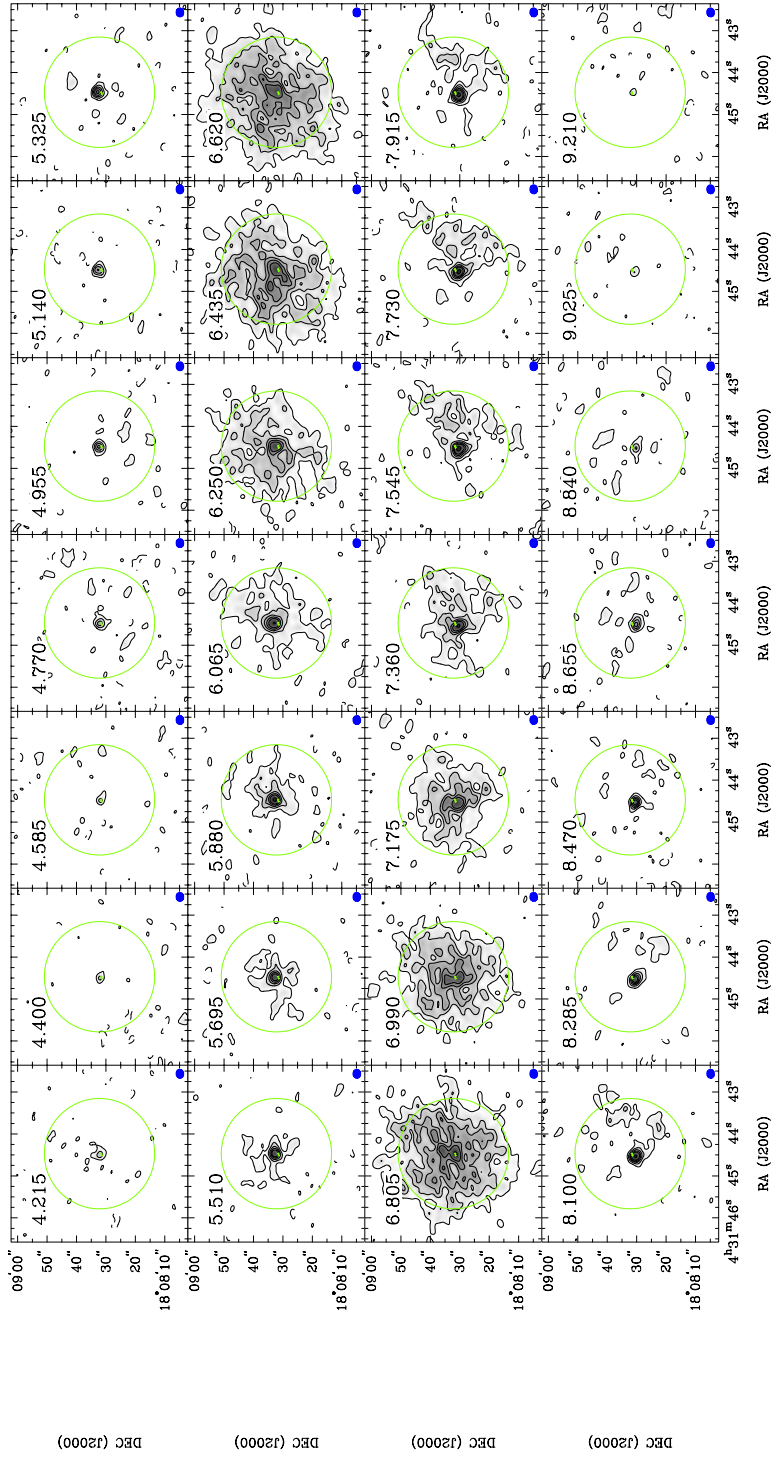


Fig. 10.— SMA+ASTE velocity channel maps of the  $\text{C}^{18}\text{O}$  (3–2) line in L1551 NE. Contour levels start from  $2\sigma$  in steps of  $2\sigma$  until  $10\sigma$ , and then in steps of  $4\sigma$  ( $1\sigma = 0.598$  K). Symbols are the same as those in Figure 9.

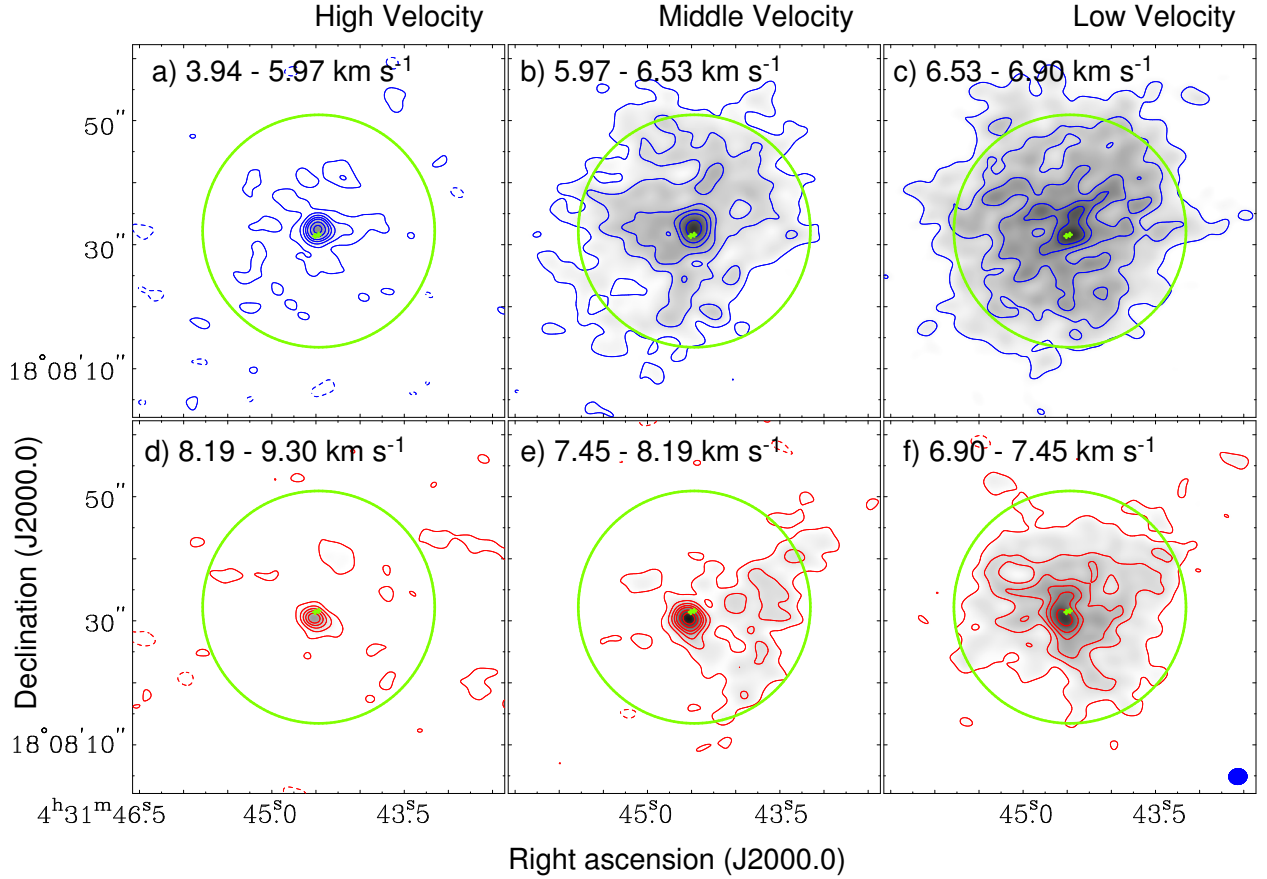


Fig. 11.— SMA+ASTE maps of the high-, middle-, and low-velocity blueshifted (blue contours) and redshifted (red contours)  $\text{C}^{18}\text{O}$  (3–2) emission in L1551 NE. Integrated velocity ranges are labeled at the top-left corners of the panels. Contour levels are in steps of  $3\sigma$  until  $15\sigma$ , and then in steps of  $5\sigma$ , where  $1\sigma$  noise levels are 0.178 K, 0.339 K, 0.420 K, 0.242 K, 0.307 K, and 0.339 K in panels (a), (b), (c), (d), (e), and (f), respectively. Symbols are the same as those in Figure 9.



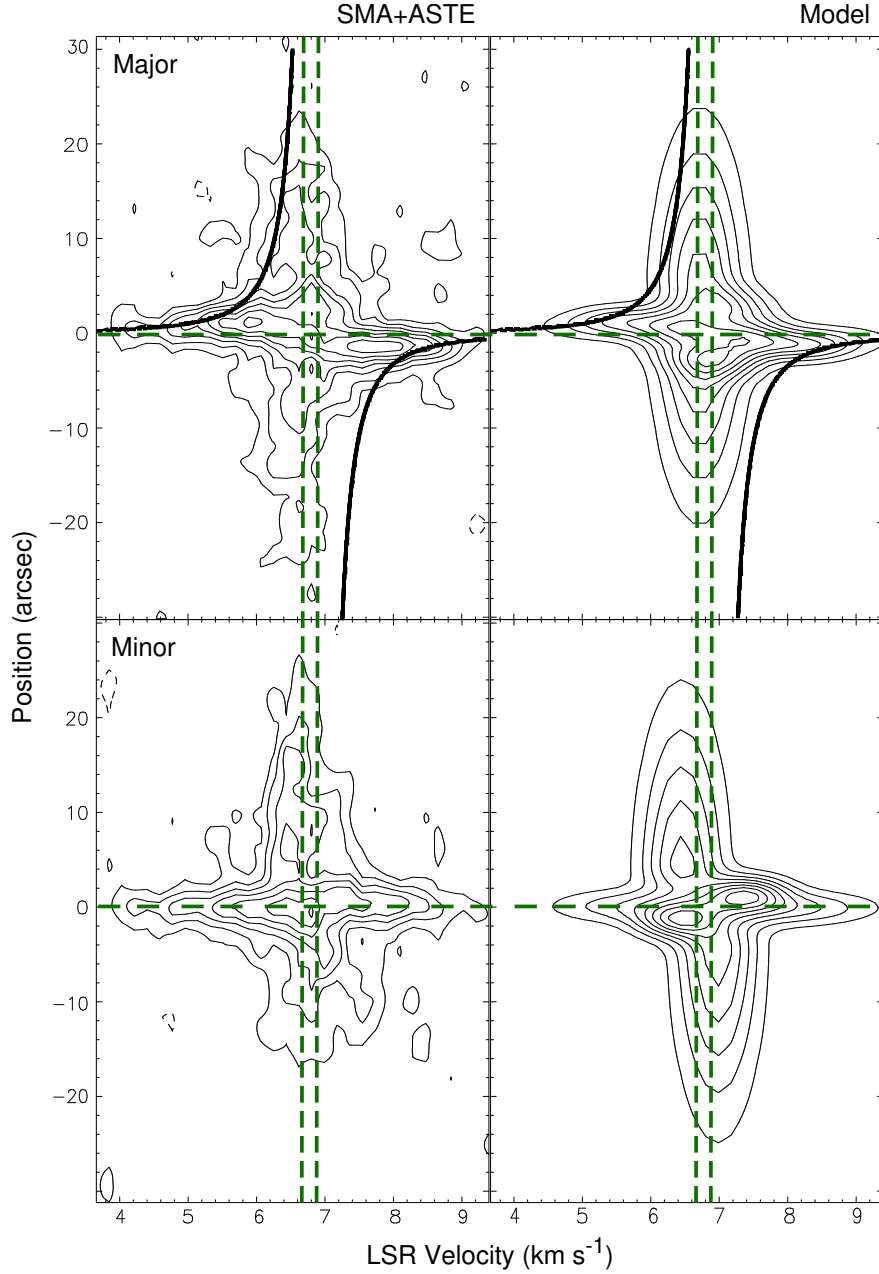


Fig. 12.— Left: SMA+ASTE P-V diagrams of the  $\text{C}^{18}\text{O}$  (3–2) emission in L1551 NE along the major (P.A.=167°; upper panel) and minor axes (P.A.=77°; lower) of the Keplerian CBD. Contour levels are in steps of  $2\sigma$  ( $1\sigma = 0.598$  K). Horizontal dashed lines denote the position of the protostellar binary (Source A), while two vertical dashed lines the systemic velocities of the extended envelope component ( $V_{\text{LSR}} = 6.7$  km s $^{-1}$ ) and the disk ( $V_{\text{LSR}} = 6.9$  km s $^{-1}$ ). Solid black curves show the Keplerian rotation curve of the disk (*i.e.*,  $M_{\star} = 0.8 M_{\odot}$  and  $i = 62^{\circ}$ ). Right: P-V diagrams of our toy model. Contour levels and symbols are the same as those in the left panel.

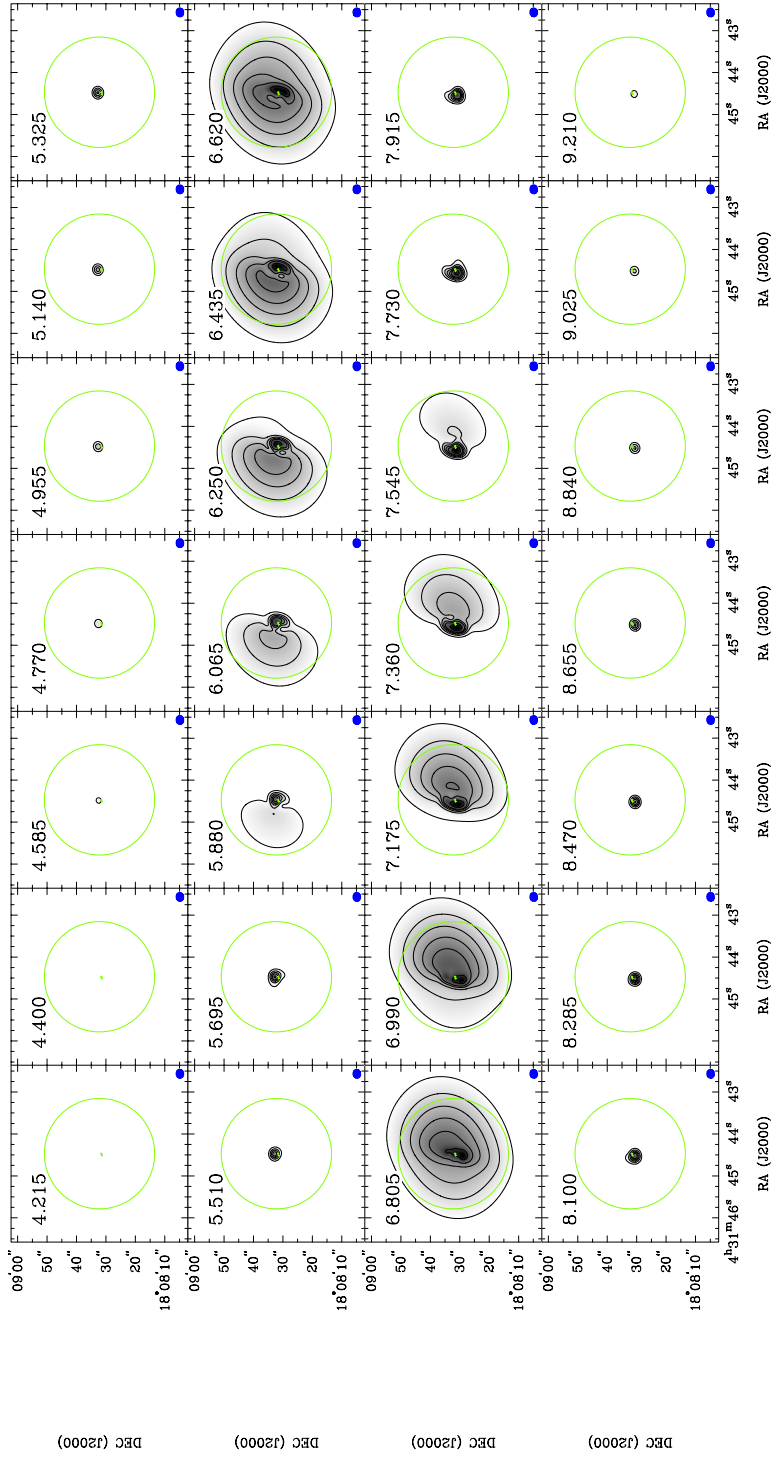


Fig. 13.— Velocity channel maps of our toy model of the  $\text{C}^{18}\text{O}$  (3–2) line in L1551 NE (see texts for details.). Velocity ranges, contour levels, and symbols are the same as those in Figure 10.

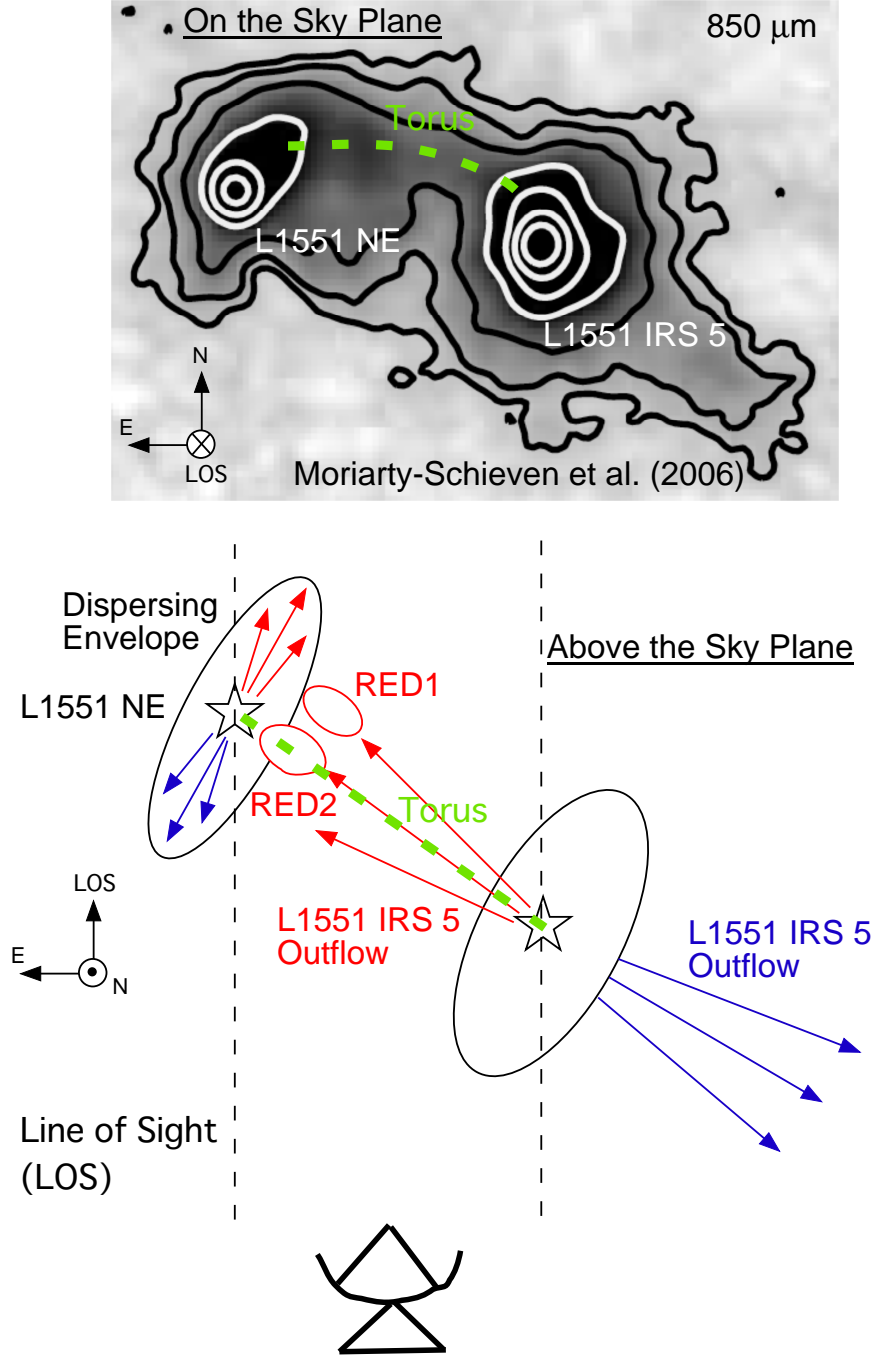


Fig. 14.— Schematic illustration of the L1551 IRS 5 / NE system. The upper figure shows the 850  $\mu\text{m}$  dust-continuum image of the L1551 region taken with SCUBA (Moriarty-Schieven et al. 2006). The lower illustration shows a schematic, anticipated view of the L1551 IRS 5 / NE system viewed from the north. Green dashed curves denote the “torus” structure of the continuum emission connecting between L1551 IRS 5 and NE.

Table 1. Resolutions and Noise Levels of the C<sup>18</sup>O (3–2) Image Cubes

Parameter	ASTE	ASTE+SMA
Beam	23''	2''.85×2''.45 (P.A. = -85°3)
Velocity Resolution	0.114 km s <sup>-1</sup>	0.185 km s <sup>-1</sup>
Noise Level	0.18 K	0.60 K

Table 2. Physical Properties of the Gas Components in L1551 NE Identified with ASTE

Component	Tracer	RA <sup>a</sup>	DEC <sup>a</sup>	$V_{LSR}$ (km s <sup>-1</sup> )	Size <sup>a</sup> (AU)	$\Delta v^b$ (km s <sup>-1</sup> )	$v_{flow}^c$ (km s <sup>-1</sup> )	$M_{LTE}^d$ ( $M_{\odot}$ )	$M_{vir}^d$ ( $M_{\odot}$ )	$p^d$ ( $M_{\odot}$ km s <sup>-1</sup> )	$E_{int}^d$ ( $\times 10^{42}$ erg)	$E_{kin}^d$ ( $\times 10^{42}$ erg)
ENV	C <sup>18</sup> O (3-2)	04 31 44.4	18 08 36.4	5.31 - 8.15	22100 $\times$ 18200	0.72	...	1.3 - 3.1	5.3	0.38 - 0.93	3.5 - 8.7	1.14 - 2.78
RED1	CS (7-6)	04 31 42.0	18 08 06.0	8.04 - 9.13	<4000	0.97	1.9	0.02 - 0.83	<1.9	0.039 - 1.574	0.10 - 4.23	0.73 - 29.74
RED2 <sup>e</sup>	<sup>13</sup> CO (3-2)	04 31 42.8	18 08 35.0	9.47 - 12.53	4300 $\times$ 4000	2.0	3.5	0.02 - 0.05	8.4	0.069 - 0.169	0.42 - 1.04	2.4 - 5.9

<sup>a</sup>Derived from two-dimensional Gaussian fittings to the moment 0 maps of the individual components. For ENV, two-component, two-dimensional Gaussian fitting is performed, and the position is defined as the peak position of the central Gaussian component, while the size is defined as the size of the outer Gaussian component.

<sup>b</sup>FWHM line widths of the spectra toward the center of the components.

<sup>c</sup>Mean velocity at the center of the components minus the velocity of the envelope component (= 6.7 km s<sup>-1</sup>).

<sup>d</sup>See texts for details.

<sup>e</sup>It is not straightforward to unambiguously separate RED2 from the other lower-velocity components in the <sup>13</sup>CO emission. Here RED2 is defined from the isolated component in the velocity higher than 9.47 km s<sup>-1</sup>.